Thin-Walled Structures 181 (2022) 110029

Contents lists available at ScienceDirect

Thin-Walled Structures

journal homepage: www.elsevier.com/locate/tws

Full length article

Experimental investigation of wire arc additively manufactured steel single-lap shear bolted connections

Xi Guo [a,*], Pinelopi Kyvelou [a], Jun Ye [a], Lip H. Teh [b], Leroy Gardner [a]

[a] Department of Civil and Environmental Engineering, Imperial College London, London SW7 2AZ, UK
[b] School of Civil, Mining and Environmental Engineering, University of Wollongong, Wollongong 2500, Australia

ARTICLE INFO

Keywords:
3D printing
Bolted connections
Curl-bearing
End-splitting
Localised tearing
Shear-out
Single-shear connections
Tilt-bearing
Wire arc additive manufacturing

ABSTRACT

An experimental investigation into the structural performance of wire arc additively manufactured (WAAM) steel single-lap shear bolted connections is presented in this paper. The steel wire had a nominal yield stress of 420 MPa. Sixty specimens of different thicknesses, printing strategies and geometric features including end distances and plate widths were tested and analysed. The shear-out, net section tension fracture, localised tearing and curl-bearing failure modes were observed and discussed, while end-splitting was also evident. Digital image correlation (DIC) was used for detailed monitoring and visualisation of the surface strain fields that developed during testing, providing valuable insight into the developed failure mechanisms. The experimental results, which generally followed the anticipated trends, were used to assess the applicability of current design specifications developed for conventional steel bolted connections to WAAM steel bolted connections. It was found that both the cold-formed steel specifications (AISI S100 and AS/NZS 4600) and the structural steel specifications (AISC 360 and EN 1993-1) devised for conventionally manufactured steel elements, could yield considerable overestimations and underestimations of the test capacities, depending on the geometry. The overestimations are caused by shortcomings in the existing design provisions for out-of-plane failure modes, which are particularly prevalent among WAAM steel connections due to their material ductility and surface undulations, which promote curling. The underestimations relate primarily to the conservatism of the shear-out provisions. Further research is underway to underpin the development of improved design provisions.

1. Introduction

Wire arc additive manufacturing (WAAM) belongs to the directed energy deposition (DED) family of additive manufacturing methods, and can be used to build large scale elements in an efficient manner [1–9]. WAAM utilises conventional welding equipment, in conjunction with robotic control, to build target components through successive deposition of layers of material. The advantages of this innovative technology over conventional manufacturing methods, which include enhanced geometric versatility, increased automation and reduced material consumption [7,10], render WAAM capable of bringing about a step-change to the modus operandi of the construction industry. However, for this potential to be fully realised, a comprehensive understanding of the structural performance of WAAM steel members and connections is required.

Bolted connections are the most common type of connection used in steel construction, in which the load may be transmitted by means of shear in the bolts and bearing in the connected parts. Four distinct modes of failure were identified by Winter [11] for bolted connections: shear-out failure, bearing failure, net section tension failure and bolt shear failure – see Fig. 1, with the latter type depending on the strength of the bolt (rather than that of the connected plates). Extensive research has been carried out on bolted connections, including tests on shear connections for tubular structures [12–14], as well as lap shear tests on cold-reduced sheet steel [15–20], high strength steel [21–23], stainless steel [24–27] and aluminium alloy [28] specimens. Several studies, particularly those featuring thin sheets under single shear, have revealed that the plates of lap connections can exhibit out-of-plane deformations, known as curling, resulting in reduced ultimate capacities [19,24,29].

In this paper, the structural performance of WAAM steel bolted connections subjected to single shear is investigated for the first time. Such connections are likely to be required in hybrid applications where 3D printed and conventional structural components are utilised in combination. Sixty WAAM specimens of two different nominal thicknesses (3 mm and 8 mm) were manufactured with varying dimensions to obtain four distinct failure modes: net section tension fracture, shear-out, localised tearing and curl-bearing failure. The effects of material

* Corresponding author.
E-mail address: x.guo19@imperial.ac.uk (X. Guo).

https://doi.org/10.1016/j.tws.2022.110029
Received 29 March 2022; Received in revised form 22 June 2022; Accepted 13 August 2022
Available online xxxx

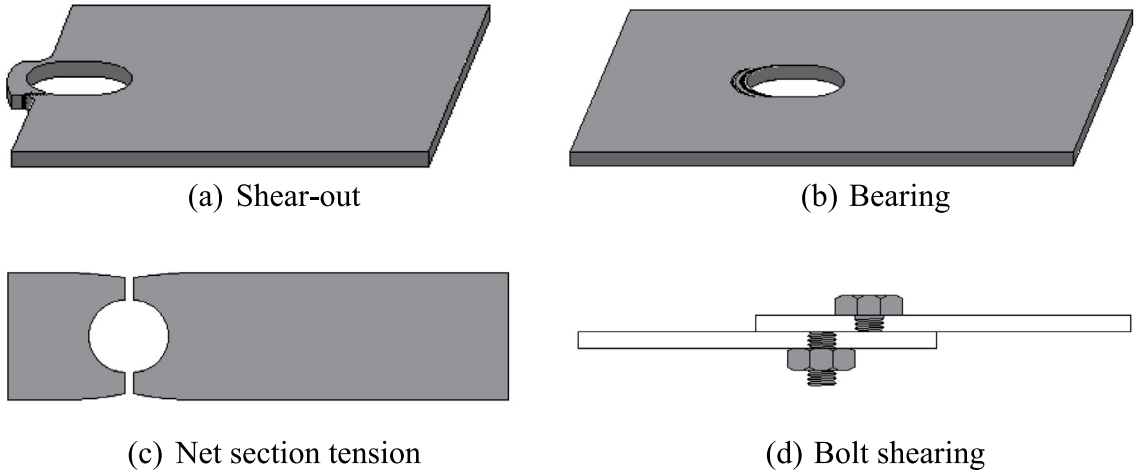

Fig. 1. Conventional failure modes for bolted connections.

Table 1
Chemical composition (% by weight) of feedstock wire, as provided by the manufacturer.

C	Si	Mn	P	S	Cr	Ni	Mo	Cu	V	Ai	Zr+Ti
0.07	0.85	1.43	0.007	0.006	0.04	0.01	0.01	0.01	0.01	0.01	0.02

Table 2
Mechanical properties (as welded) of feedstock wire, as provided by the manufacturer.

Yield strength (MPa)	Ultimate tensile strength (MPa)	Elongation A5 (%)	Impact energy at 40 °C (J)
471	580	25	73

Table 3
Printing parameters for WAAM material of two nominal thicknesses t_{nom}.

Printing parameter	t_{nom}	
	3mm	8 mm
Wire diameter (mm)	0.8	1.2
Travel speed (mm/s)	8	8
Wire feed speed (m/min)	3	4
Welding voltage (V)	14.8	24.8
Welding current (A)	54	130
Gas flow rate (L/min)	14	16
Shielding gas	80% Ar + 20% CO_2	
Welding mode	Short-arc	Pulsed
Dwell time (s)	30	30

anisotropy and of the surface undulations inherent to the WAAM process on the structural response of the examined connections were investigated by testing specimens with two different angles (0° and 90°) between the print layer orientation and the axis of loading. The particular geometric features of all specimens were captured by means of laser scanning, while digital image correlation (DIC) was employed to monitor the surface strain fields during testing. The observed failure modes are discussed herein and the applicability of current steel structure specifications [30–34] to the design of WAAM connections is assessed.

2. Manufacturing and geometric measurements of test specimens

The test specimens were manufactured by MX3D [35], using their proprietary multi-axis robotic WAAM technology. Oval tubes of 3 mm and 8 mm nominal thickness, as shown in Fig. 2, were printed using steel welding wire ER70S-6 (EN ISO 14341-A G 42 3 M21 3Si1). The

Fig. 2. WAAM oval tubes from which test specimens were cut.

first letter G indicates gas-shielded metal arc welding; the number 42 denotes a minimum yield strength of 420 MPa, a tensile strength between 500 MPa and 640 MPa and a minimum elongation at fracture of 20%; the number 3 indicates that at a temperature of −30 °C a minimum average impact energy of 47 J is achieved; the notation M21 is the classification of the shielding gas; and the last notation 3Si1 refers to the chemical composition of the wire electrode [36]. The chemical composition and the mechanical properties of the feedstock material, as reported by the manufacturer, are presented in Tables 1 and 2, respectively, and the printing parameters employed during the WAAM process are reported in Table 3. The oval tubes provided a stable build geometry and are more efficient to print. Test specimens were extracted from the flat sides of the tubes using a water jet cutter, as shown in Fig. 3, and were then sandblasted with glass beads to remove any welding soot from the WAAM process.

Sixty WAAM lap shear specimens of two different nominal thicknesses and two print layer orientations were fabricated, the basic configuration of which is shown in Fig. 4, where d_0 is the bolt hole diameter, e_1 is the end distance between the centre of the bolt hole and the end of the WAAM plate, b is the plate width and x and y represent the directions perpendicular and parallel to the loading direction, respectively. The lengths of the specimens were approximately three times their respective widths, varying from 190 mm to 390 mm.

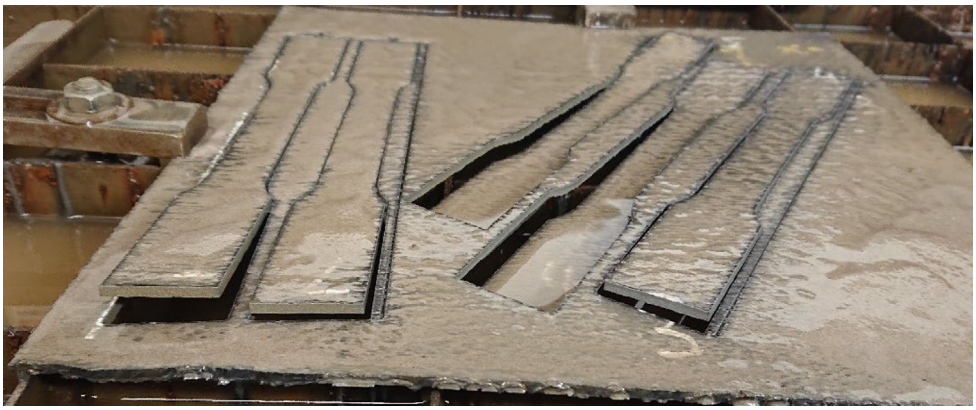

Fig. 3. Specimens cut from the flat sides of the tubes using a water jet cutter.

Table 4
Measured geometric properties of test specimens.

Specimen	Bolttype	t(mm)	d_0 (mm)	b(mm)	e_1 (mm)
S3-55-27-0	M16	2.7	18.0	55.1	26.9
S3-45-27-0	M16	3.0	17.8	45.4	27.3
S3-45-36-0	M16	3.0	17.7	45.4	36.3
S3-35-27-0	M16	2.7	17.9	34.8	26.8
S3-65-18-0	M16	2.8	17.8	65.5	18.2
S3-65-21.6–0	M16	2.9	17.8	65.4	21.6
S3-65-27-0	M16	2.9	17.8	65.3	27.0
S3-65-32.4–0	M16	2.8	17.8	65.4	32.5
S3-65-36-0	M16	2.8	17.8	65.5	36.3
S3-85-33-0	M20	2.8	21.8	85.5	33.3
S3-85-44-0	M20	2.7	21.7	85.4	44.3
S3-105-33-0	M20	2.6	22.2	105.0	32.9
S3-105-39.6–0	M20	2.6	22.6	105.0	39.3
S3-105-44-0	M20	2.7	22.2	105.1	44.1
S3-145-44.2–0	M24	2.7	26.2	144.0	43.8
S3-145-78-0	M24	2.7	26.3	143.4	78.2
S3-145-104-0	M24	2.6	26.3	144.2	104.2
S8-45-39-0	M24	7.3	26.4	45.1	38.9
S8-55-39-0	M24	7.5	26.2	55.0	39.1
S8-65-39-0	M24	7.5	26.2	64.7	39.1
S8-75-39-0	M24	7.6	25.9	75.0	39.0
S8-95-26-0	M24	7.5	25.9	95.1	26.1
S8-95-33.8–0	M24	7.6	26.1	95.3	33.9
S8-95-39-0	M24	7.5	25.9	95.3	39.2
S8-95-65-0	M24	7.4	25.9	94.9	65.0
S8-95-78-0	M24	7.4	25.9	94.9	78.3
S8-117-32-0	M30	7.4	32.0	117.2	32.1
S8-117-48-0	M30	7.6	31.7	117.1	47.8
S8-117-80-0	M30	7.5	31.8	117.3	79.9
S8-117-96-0	M30	7.6	31.9	117.3	96.0
S3-55-27-90	M16	2.7	18.1	54.5	26.8
S3-45-27-90	M16	2.9	17.9	45.5	27.4
S3-45-36-90	M16	2.9	17.8	45.3	36.3
S3-35-27-90	M16	2.7	18.1	34.8	26.9
S3-65-18-90	M16	3.0	17.8	65.5	18.3
S3-65-21.6–90	M16	2.9	17.8	65.3	21.8
S3-65-27-90	M16	2.9	17.7	65.3	27.0
S3-65-32.4–90	M16	2.9	17.8	65.3	32.4
S3-65-36-90	M16	2.9	17.8	65.1	36.3
S3-85-33-90	M20	2.8	21.9	85.6	33.4

(*continued on next page*)

Table 4 (*continued*).

Specimen	Bolttype	t(mm)	d_0 (mm)	b(mm)	e_1 (mm)
S3-85-44-90	M20	2.8	21.9	85.6	44.4
S3-105-33-90	M20	2.8	22.2	105.1	33.0
S3-105-39.6–90	M20	2.8	22.1	105.1	39.0
S3-105-44-90	M20	2.8	22.1	104.9	43.6
S3-145-44.2–90	M24	2.7	25.9	144.0	40.8
S3-145-78-90	M24	2.7	26.2	145.1	78.1
S3-145-104-90	M24	2.7	26.2	143.9	103.4
S8-45-39-90	M24	7.4	26.2	44.7	38.8
S8-55-39-90	M24	7.5	26.2	54.9	38.9
S8-65-39-90	M24	7.3	26.2	64.9	39.2
S8-75-39-90	M24	7.5	26.2	75.2	38.9
S8-95-26-90	M24	7.7	25.9	95.2	26.1
S8-95-33.8–90	M24	7.6	26.0	95.2	34.0
S8-95-39-90	M24	7.7	25.9	95.0	39.2
S8-95-65-90	M24	7.7	25.8	95.1	65.1
S8-95-78-90	M24	7.6	25.9	94.9	78.2
S8-117-32-90	M30	7.5	32.0	117.2	32.2
S8-117-48-90	M30	7.5	31.9	117.2	48.3
S8-117-80-90	M30	7.6	31.9	117.2	80.2
S8-117-96-90	M30	7.6	32.0	117.2	96.2

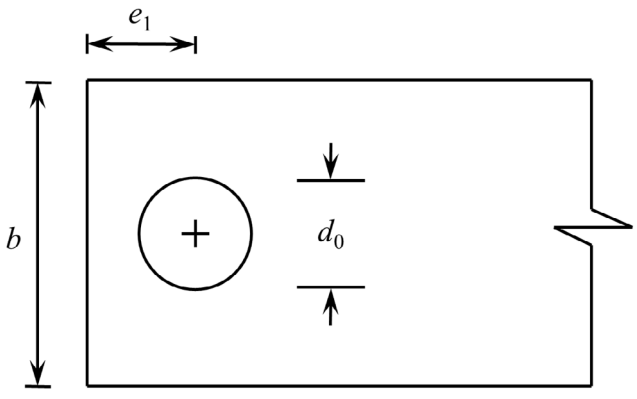

Fig. 4. Basic geometry of test specimens.

The labelling for the test specimens begins with the letter S (for shear) followed immediately by the nominal thickness in mm, a hyphen, the nominal width b in mm, a second hyphen, the end distance e_1 in mm, a third hyphen and, finally, the angle in degrees between the axis of loading and the print layer orientation – see Fig. 5. For example,

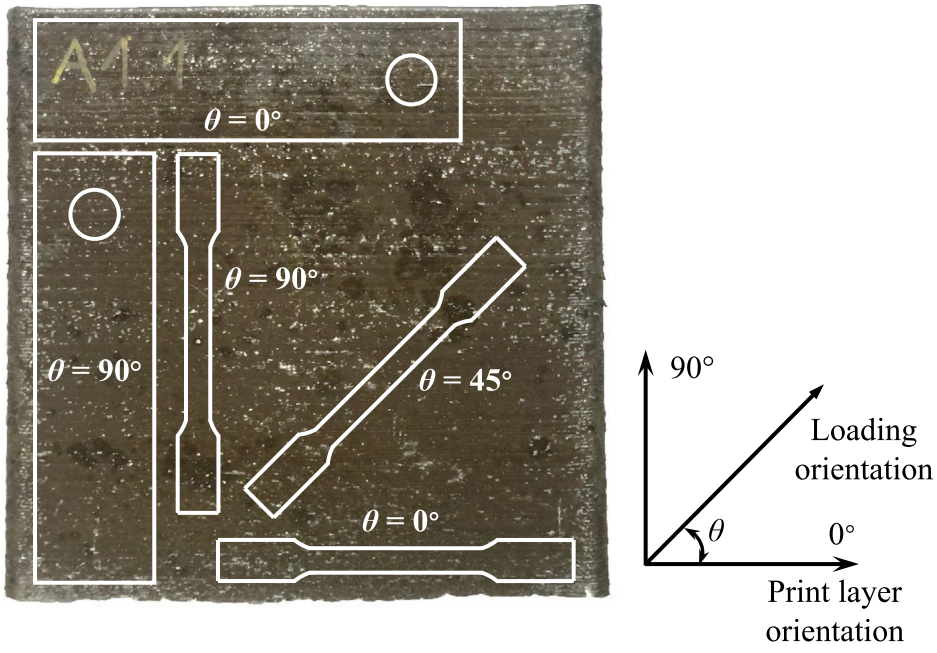

Fig. 5. Orientation of tensile coupons and lap specimens extracted from WAAM plates relative to print layer orientation.

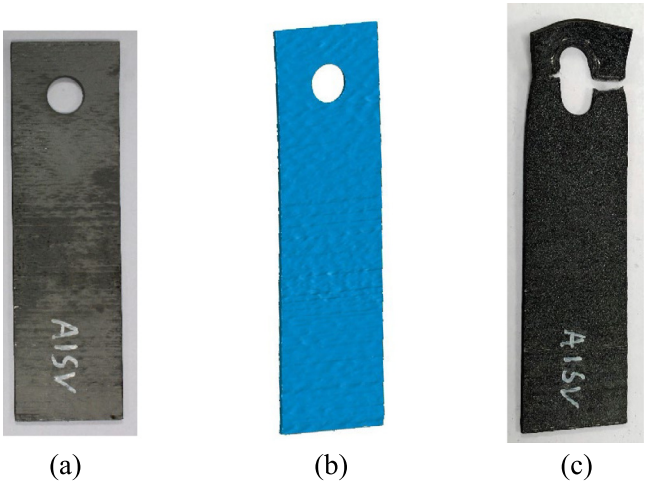

Fig. 6. Typical test specimen: (a) following sandblasting, (b) digital model from laser scan and (c) after testing.

Specimen S3-55-27-90 is a lap shear specimen with nominal values of thickness, width and end distance equal to 3 mm, 55 mm and 27 mm, respectively, with the axis of loading perpendicular to the print layer orientation.

The width b, end distance e_1 and bolt hole diameter d_0 of each test specimen were measured using Vernier callipers; the results are presented in Table 4. However, due to the inherent surface undulations of as-built WAAM specimens, thickness measurements taken using conventional tools can be inaccurate [6,8]. Therefore, 3D laser scanning was employed in the present work. A FARO Design ScanArm 2.0, capable of recording 600,000 points per second with an accuracy of 0.075 mm [37], was used to obtain scans of both surfaces of each lap specimen; which were then merged into a single model represented as a point cloud in the software Geomagic Wrap [38]. The point cloud was subsequently inter-connected to form a polygonal mesh and a 3D CAD model, which was then imported into Rhino 3D [39] as an STL file to determine the average thickness of the specimen [6,8]. The values of the average thickness t of all specimens are given in Table 4. Photographs of a typical specimen before and after testing, together with the corresponding 3D CAD model following laser scanning, are shown in Fig. 6.

Table 5
Measured mechanical properties obtained from machined tensile coupons.

t_{nom}(mm)	θ(°)	E(GPa)	f_y(MPa)	f_u (MPa)	ε_u	ε_f
3	0	211	405	503	0.12	0.26
	45	210	366	482	0.16	0.39
	90	209	372	484	0.16	0.35
8	0	214	292	434	0.22	0.40
	45	212	329	440	0.21	0.38
	90	212	319	444	0.17	0.30

3. Material tests

Twenty nine tensile coupon tests were conducted to determine the mechanical properties of the WAAM material. Anisotropy was investigated by testing coupons extracted from the WAAM plates at angles of 0°, 45° and 90° to the print layer orientation, as illustrated in Fig. 5. The influence of the undulating as-built geometry on the mechanical response was examined by testing as-built and machined coupons, with the surface undulations of the latter having been removed using an end mill. Following their extraction from the parent plates using a water jet cutter, the coupons were sandblasted and laser scanned to obtain their average thickness and cross-sectional area.

The material tests were conducted in accordance with EN ISO 6892-1 [40], using a 250 kN Instron 8800 testing machine at a constant strain rate of 0.00007 s^{-1}. A four-camera LaVision digital image correlation (DIC) system was employed to accurately monitor the surface strain fields on both sides of each coupon, over the parallel length. The acquired images, recorded at a frequency of 1 Hz, were processed in the software Davis [41].

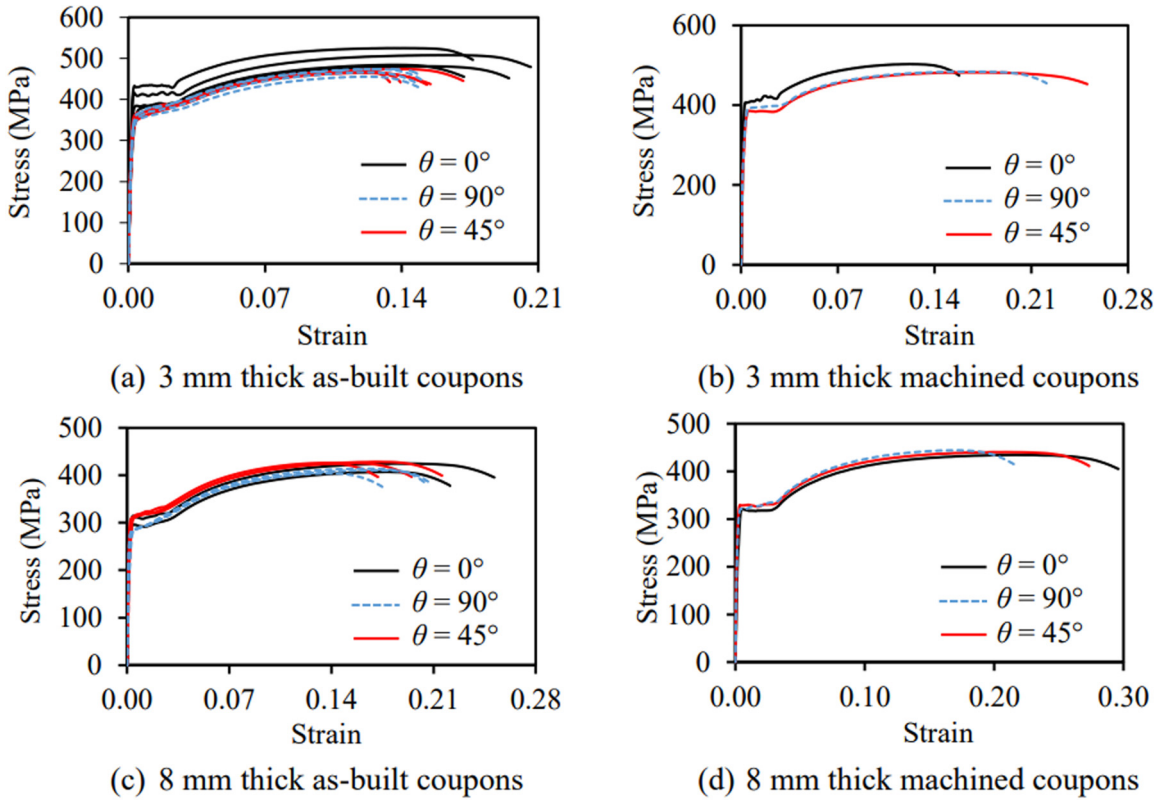

Fig. 7. Stress–strain curves obtained from tensile coupon tests.

Table 6
Measured effective mechanical properties obtained from as-built tensile coupons.

t_{nom}(mm)	θ(°)	E_{eff}(GPa)	$f_{y,eff}$(MPa)	$f_{u,eff}$ (MPa)	$\varepsilon_{u,eff}$	$\varepsilon_{f,eff}$
3	0	196	408	508	0.15	0.26
	45	194	356	469	0.12	0.24
	90	196	355	467	0.13	0.22
8	0	213	306	416	0.18	0.36
	45	213	304	427	0.15	0.27
	90	218	278	409	0.16	0.24

A summary of the average mechanical properties in each loading direction obtained from the machined coupon tests by loading direction (i.e. θ = 0°, 45°, 90°) is presented in Table 5, where E is the Young's modulus, f_y is the yield strength defined as the 0.2% proof stress, f_u is the ultimate tensile strength, ε_u is the strain at f_u and ε_f is the fracture strain, determined over a standard gauge length of $5.65\sqrt{A}$, where A is the mean cross-section area along the parallel length [40]. The results from the as-built coupon tests are provided in Table 6, where the subscript 'eff' has been added to the variables to reflect the effective nature of the mechanical properties, as influenced by the as-built geometry [8]. The stress–strain curves of all coupons, grouped by nominal thickness and surface condition (i.e. machined and as-built), are presented in Fig. 7.

The material anisotropy was found to be rather mild, with the variations in the yield and ultimate tensile strengths being within 15%. The influence of the surface undulations on the mechanical properties of the examined WAAM material is evident, with the Young's modulus, yield and ultimate strengths of the as-built coupons being up to 10% lower than those of the machined coupons. The strength of the thicker material, both for the machined and as-built coupons, was found to be consistently lower than the strength of the thinner material, with differences of up to about 40% and 20% for the yield and ultimate tensile strengths, respectively – see Tables Tables 5 and 6; this is attributed to the slower cooling rate of the thicker material [42].

4. Lap shear connection tests

4.1. Test setup

An overview of the test setup employed for the lap shear tests is illustrated in Fig. 8. Each test comprised a WAAM plate (i.e. the test specimen) connected to a conventional high strength steel (HSS) plate by means of a single fully threaded bolt in a 2 mm clearance bolt hole [32]. The bolt head and nut were finger-tightened to ensure contact at the interface of the plates, while limiting the influence of friction [43]. Note that the WAAM and HSS plates were of the same dimensions, ensuring the occurrence of failure within the (weaker) WAAM plate. The size (varying from M16 to M30) and grade (grade 12.9) of the bolts were selected such that shear failure of the bolts would be avoided.

All tests were conducted using a 600 kN Instron testing machine. The specimens were loaded using displacement control at a constant rate of 0.8 mm/min. A four-camera DIC system was employed to record the displacements and strain fields of both sides of the specimens, which were first painted black and then sprayed with a random white speckle pattern prior to testing to provide features for the DIC system to monitor – see Fig. 8.

4.2. Failure modes

The observed failure modes of all tested specimens are reported in Table 7, where shear-out, net section tension, localised tearing, end-splitting and curl-bearing (see Section 4.2.4) failures are denoted by SO, NS, LT, ES and CB, respectively.

4.2.1. Shear-out, net section tension and bearing failures

As expected, shear-out failures developed in the specimens with short end distances e_1 and large plate widths b – see Fig. 9(a), while net section tension failures occurred in the specimens with larger end

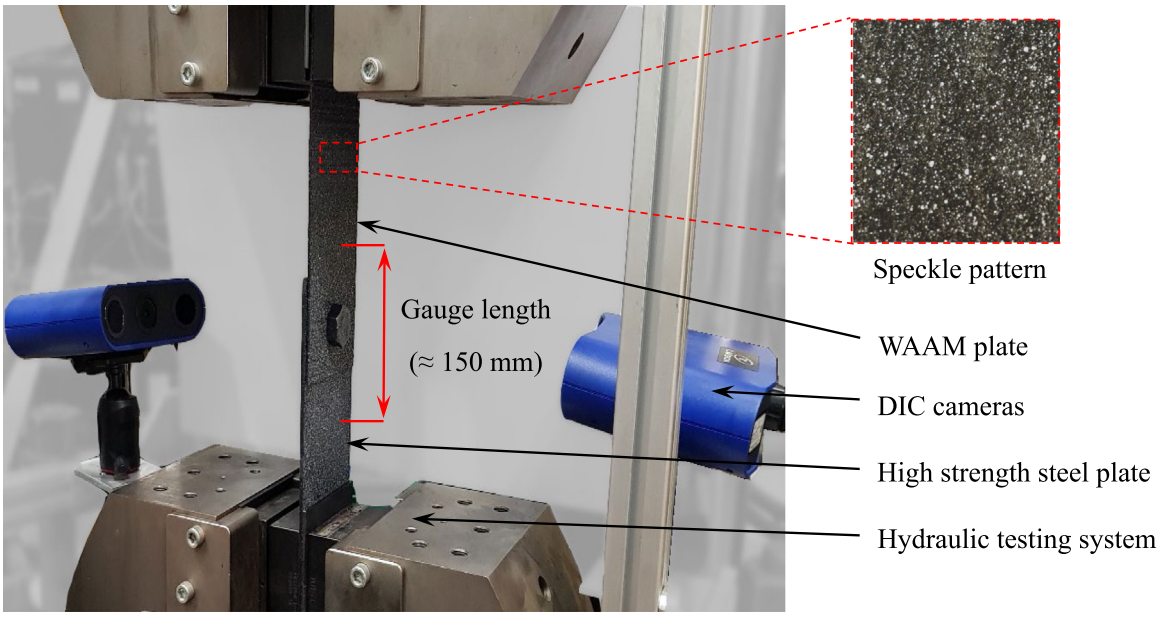

Fig. 8. Experimental setup for lap shear connection tests.

Table 7
Summary of experimental results (FM = failure mode) and comparisons with design standards (SO: shear-out; NS: net section; B: bearing; LT: localised tearing; ES: end-splitting and CB: curl-bearing failure, in brackets if different from test results).

Specimen	Test			AISI S100 Eqs. (1)–(3)		AISC 360 Eqs. (4)–(6)		AS/NZS 4600 Eqs. (1), (3) and (10)		Eurocode 3 Eqs. (7) and (9)		Eq. (13)	Eq. (14)
	P_u (kN)	FM	Curling	$\frac{P_u}{P_{AISI}}$	FM	$\frac{P_u}{P_{AISC}}$	FM	$\frac{P_u}{P_{AS/NZS}}$	FM	$\frac{P_u}{P_{EC3}}$	FM	$\frac{P_u}{P_{s,eq.13}}$	$\frac{P_u}{P_{1b,eq.14}}$
S3-35-27-90	21.44	NS		1.07	NS	1.01	NS	1.07	NS	1.01	NS	N/A	N/A
S3-35-27-0	21.53	NS		1.02	NS	0.96	NS	1.02	NS	0.96	NS	N/A	N/A
S3-45-27-90	35.51	NS+LT	✓	1.17	(SO)	0.94	NS	1.00	NS	1.06	(SO)	N/A	0.98
S3-45-27-0	37.13	NS+LT	✓	1.14	(SO)	0.91	(SO)	0.97	NS	1.02	(SO)	N/A	0.95
S3-45-36-90	36.12	NS+LT	✓	1.03	NS	0.96	NS	1.03	NS	0.96	NS	N/A	1.01
S3-45-36-0	37.17	NS+LT	✓	0.96	NS	0.90	NS	0.96	NS	0.90	NS	N/A	0.94
S3-55-27-90	36.30	LT	✓	1.38	(SO)	1.10	(SO)	1.09	(SO)	1.24	(SO)	N/A	1.10
S3-55-27-0	39.28	LT	✓	1.38	(SO)	1.10	(SO)	1.10	(SO)	1.24	(SO)	N/A	1.11
S3-65-18-90	25.97	SO		1.67	SO	1.34	SO	1.03	SO	1.15	SO	1.03	N/A
S3-65-18-0	25.08	SO		1.59	SO	1.27	SO	0.97	SO	1.08	SO	0.98	N/A
S3-65-21.6–90	31.12	SO		1.48	SO	1.19	SO	1.05	SO	1.17	SO	1.02	N/A
S3-65-21.6–0	31.70	SO		1.43	SO	1.15	SO	1.01	SO	1.13	SO	0.98	N/A
S3-65-27-90	43.95	LT	✓	1.49	(SO)	1.19	(SO)	1.20	(SO)	1.33	(SO)	N/A	1.13
S3-65-27-0	42.59	SO	✓	1.33	SO	1.07	SO	1.07	SO	1.19	SO	1.01	N/A
S3-65-32.4–90	44.30	LT	✓	1.15	(SO)	0.92	(SO)	1.00	(SO)	1.11	(SO)	N/A	1.13
S3-65-32.4–0	43.71	LT	✓	1.10	(SO)	0.88	(SO)	0.96	(SO)	1.07	(SO)	N/A	1.09
S3-65-36-90	42.50	LT	✓	0.96	(SO)	0.77	(SO)	0.88	(B)	0.97	(SO)	N/A	1.10
S3-65-36-0	43.10	LT	✓	0.92	(SO)	0.74	(SO)	0.84	(B)	0.93	(SO)	N/A	1.06
S3-85-33-90	42.78	LT	✓	1.24	(SO)	0.99	(SO)	1.00	(SO)	1.09	(SO)	N/A	1.00
S3-85-33-0	48.88	LT	✓	1.32	(SO)	1.05	(SO)	1.06	(SO)	1.16	(SO)	N/A	1.07
S3-85-44-90	49.41	LT	✓	0.96	(SO)	0.77	(SO)	0.87	(SO)	0.95	(SO)	N/A	1.16
S3-85-44-0	50.46	LT	✓	0.92	(SO)	0.73	(SO)	0.83	(SO)	0.90	(SO)	N/A	1.11
S3-105-33-90	47.54	LT	✓	1.41	(SO)	1.13	(SO)	1.12	(SO)	1.25	(SO)	N/A	1.07
S3-105-33-0	47.67	SO	✓	1.39	SO	1.11	SO	1.11	SO	1.22	SO	1.04	N/A
S3-105-39.6–90	53.21	LT	✓	1.20	(SO)	0.96	(SO)	1.03	(SO)	1.14	(SO)	N/A	1.15
S3-105-39.6–0	48.02	LT	✓	1.10	(SO)	0.88	(SO)	0.94	(SO)	1.06	(SO)	N/A	1.08
S3-105-44-90	50.88	LT	✓	0.99	(SO)	0.79	(SO)	0.89	(SO)	0.98	(SO)	N/A	1.11
S3-105-44-0	51.12	LT	✓	0.96	(SO)	0.77	(SO)	0.86	(SO)	0.95	(SO)	N/A	1.10
S3-145-44.2–90	46.30	LT	✓	1.10	(SO)	0.88	(SO)	0.90	(SO)	0.97	(SO)	N/A	0.91

(*continued on next page*)

Table 7 (*continued*).

Specimen	Test			AISI S100 Eqs. (1)–(3)		AISC 360 Eqs. (4)–(6)		AS/NZS 4600 Eqs. (1), (3) and (10)		Eurocode 3 Eqs. (7) and (9)		Eq. (13)	Eq. (14)
	P_u (kN)	FM	Curling	$\frac{P_u}{P_{AISI}}$	FM	$\frac{P_u}{P_{AISC}}$	FM	$\frac{P_u}{P_{AS/NZS}}$	FM	$\frac{P_u}{P_{EC3}}$	FM	$\frac{P_u}{P_{s,eq.13}}$	$\frac{P_u}{P_{tb,eq.14}}$
S3-145-44.2–0	49.32	LT	✓	1.01	(SO)	0.81	(SO)	0.85	(SO)	0.92	(SO)	N/A	0.93
S3-145-78-90	56.81	CB	✓	0.83	(B)	0.62	(B)	0.83	(B)	0.63	(SO)	N/A	1.12
S3-145-78-0	57.03	CB	✓	0.77	(B)	0.58	(B)	0.77	(B)	0.59	(SO)	N/A	1.04
S3-145-104-90	55.88	CB	✓	0.83	(B)	0.62	(B)	0.83	(B)	0.62	(B)	N/A	1.12
S3-145-104-0	54.34	CB	✓	0.77	(B)	0.58	(B)	0.77	(B)	0.58	(B)	N/A	1.05
S8-45-39-90	62.71	NS		1.18	NS	1.12	NS	1.18	NS	1.12	NS	N/A	N/A
S8-45-39-0	60.44	NS		1.13	NS	1.07	NS	1.13	NS	1.07	NS	N/A	N/A
S8-55-39-90	95.75	NS		1.15	NS	1.08	NS	1.15	NS	1.08	NS	N/A	N/A
S8-55-39-0	101.11	NS		1.20	NS	1.13	NS	1.20	NS	1.13	NS	N/A	N/A
S8-65-39-90	118.77	NS		1.27	(SO)	1.03	NS	1.10	NS	1.11	(SO)	N/A	N/A
S8-65-39-0	123.78	NS		1.28	(SO)	1.03	NS	1.10	NS	1.11	(SO)	N/A	N/A
S8-75-39-90	133.38	ES		1.39	(SO)	1.12	(SO)	1.11	(SO)	1.21	(SO)	1.05	N/A
S8-75-39-0	146.77	ES+SO		1.49	SO	1.19	SO	1.19	SO	1.29	SO	1.12	N/A
S8-95-26-90	84.56	SO		1.70	SO	1.36	SO	1.03	SO	1.11	SO	1.03	N/A
S8-95-26-0	88.61	SO		1.79	SO	1.43	SO	1.08	SO	1.17	SO	1.08	N/A
S8-95-33.8–90	118.04	SO		1.51	SO	1.21	SO	1.12	SO	1.21	SO	1.07	N/A
S8-95-33.8–0	119.37	SO		1.51	SO	1.21	SO	1.12	SO	1.21	SO	1.07	N/A
S8-95-39-90	140.86	SO+ES		1.42	SO	1.13	SO	1.14	SO	1.23	SO	1.07	N/A
S8-95-39-0	135.59	SO+ES		1.38	SO	1.10	SO	1.11	SO	1.19	SO	1.04	N/A
S8-95-65-90	194.76	LT	✓	1.14	(B)	0.89	(NS)	1.14	(B)	1.02	(SO)	N/A	1.18
S8-95-65-0	174.51	LT	✓	1.05	(B)	0.82	(NS)	1.05	(B)	0.94	(SO)	N/A	1.11
S8-95-78-90	178.62	LT	✓	1.07	(B)	0.83	(NS)	1.07	(B)	0.83	(NS)	N/A	1.11
S8-95-78-0	191.19	LT	✓	1.14	(B)	0.89	(NS)	1.14	(B)	0.89	(NS)	N/A	1.20
S8-117-32-90	102.45	SO		1.73	SO	1.38	SO	1.04	SO	1.11	SO	1.04	N/A
S8-117-32-0	101.86	SO		1.70	SO	1.36	SO	1.02	SO	1.09	SO	1.03	N/A
S8-117-48-90	162.28	ES		1.35	(SO)	1.08	(SO)	1.09	(SO)	1.16	(SO)	1.02	N/A
S8-117-48-0	168.14	ES		1.39	(SO)	1.12	(SO)	1.12	(SO)	1.18	(SO)	1.05	N/A
S8-117-80-90	223.89	LT	✓	1.06	(B)	0.84	(NS)	1.06	(B)	0.95	(SO)	N/A	1.20
S8-117-80-0	210.80	LT	✓	1.00	(B)	0.79	(NS)	1.00	(B)	0.89	(SO)	N/A	1.13
S8-117-96-90	208.02	LT	✓	1.00	(B)	0.79	(NS)	1.00	(B)	0.79	(NS)	N/A	1.13
S8-117-96-0	213.78	LT	✓	1.00	(B)	0.79	(NS)	1.00	(B)	0.79	(NS)	N/A	1.12
Mean				1.22		0.99		1.02		1.04		1.04	1.10
COV				0.21		0.22		0.11		0.17		0.03	0.06

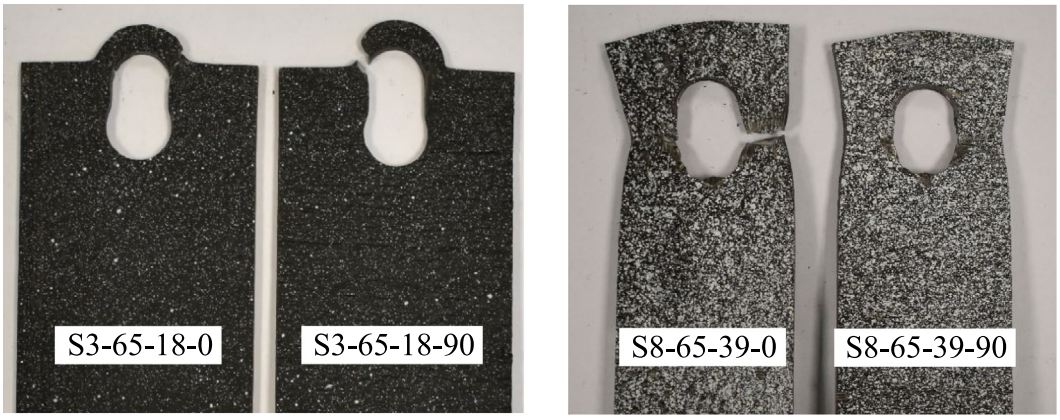

Fig. 9. Conventional failure modes: (a) shear-out and (b) net section tension.

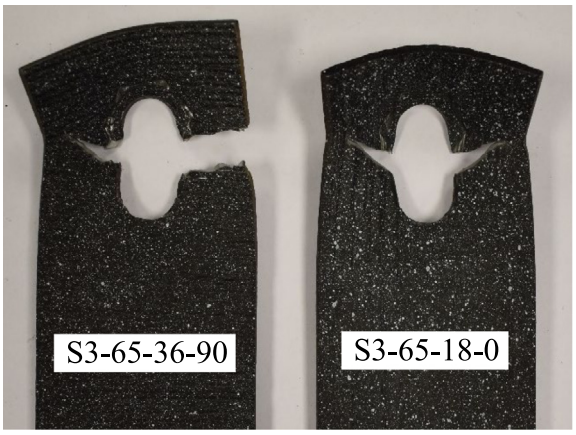

Fig. 10. Localised tearing failure.

distances and narrower widths – see Fig. 9(b). Purely bearing failures did not occur in the single-shear lap tests because of the tilting of the bolt and the curling of the plate. Instead, localised tearing or curl-bearing failure developed where the end distance and the width of the plate were sufficiently large.

4.2.2. Localised tearing failure

The failure mode shown in Fig. 10, which is associated with fracture away from the minimum net section (i.e. at the centre of the bolt hole) combined with significant out-of-plane deformations, is referred to as localised tearing and was first identified by Rogers and Hancock [19]. Localised tearing develops in elements made of ductile mild steel and can be viewed as a characteristic of localised bearing stress [19]. Note that particular attention is required to distinguish localised tearing from net section tension failure. Rogers and Hancock [19] pointed out that a lack of necking across the net section, which is characteristic of a net section tension failure, is an indication of a localised tearing failure.

The evolution of tensile strain fields in typical cases of localised tearing and of net section tension failures are presented in Figs. 11 and 12, respectively. In Fig. 11(a), a butterfly shaped strain distribution can be observed at the later stages of loading, eventually leading to fracture away from the minimum net section, as shown in Fig. 11(b). In Fig. 12, where a typical case of net section tension failure is shown, the butterfly shaped strain distribution was only partially developed when necking and subsequently rupture took place at the minimum net section, as shown in Fig. 9(b).

4.2.3. Tilt-bearing failure

Tilt-bearing [44] is a mode of failure characterised by tilting of the bolt head or nut, which punches through the plate on the upstream side of the bolt hole, typically developing in lap tests under single shear when washers are not used – see Fig. 14(b). Although tilting of the bolts was observed in the tested specimens, tilt-bearing failure did not occur. This outcome is attributed to the configuration of the test specimens and the good ductility of the studied WAAM steel, resulting in large deformations of the bolt hole and thus avoiding the bolt head (or nut) punching through the upstream side of the connected sheet – see Fig. 14(c).

4.2.4. Curling and curl-bearing failure

The out-of-plane deformation mode known as curling (as distinct from curl-bearing failure, although this failure mode must be accompanied by curling) was observed for most specimens. As expected, curling was more pronounced in the thinner (i.e. 3 mm thick) plates. Although, in most cases, curling was not the direct cause of failure, in the tests of the thin plates where the end distances were extremely large, severe curling resulted in the bolt head penetrating into the lap plate downstream of the bolt hole – see Fig. 15. This failure mode is referred to as curl-bearing failure in this paper, and to the authors' knowledge, has not been previously defined in the literature. In a sense, the curl-bearing failure mode is the "mirror" mode of the tilt-bearing failure mode, which involves the bolt head punching through the connected plate upstream as the bolt tilts backwards. They therefore share a similar fracture mechanism.

4.2.5. End-splitting failure

End-splitting failure is characterised by in-plane bending and transverse tensile fracture at the specimen end. This mode of failure has been reported by several researchers [22,23,45–48] and was also observed among the specimens tested herein. It has been shown that the occurrence of either shear-out or end-splitting failure can be sensitive to the method used to cut the connected steel sheets [45,47].

The strain fields recorded by the DIC system for a specimen (specimen S8-117-48-90) that displayed end-splitting failure are illustrated in Fig. 13, where ε_{yy} and ε_{xx} denote the longitudinal and the transverse tensile strains, respectively. It can be observed that this failure mode is characterised by high localised transverse tensile strains ε_{xx} downstream of the bolt hole leading to tensile fracture at the plate end.

4.2.6. Transition between failure modes

The transition between the different failure modes has been examined herein by varying the geometric proportions of the test specimens and carefully inspecting the exhibited failure mechanisms. As shown in Fig. 16, increasing the plate width b while keeping the end distance e_1 constant resulted in a transition from net section tension failure to end-splitting and, eventually, shear-out failure. Similarly, as shown in Figs. 17 and 18, increasing the end distance e_1 for specimens with the same width b led to a failure mode transition from shear-out to end-splitting and, then, to localised tearing failure.

4.2.7. Influence of print orientation

The angle θ between the axis of loading and the print layer orientation was not found to have a significant influence on the failure modes of most specimens, as shown in Figs. 9 and 10. However, some specimens of the same nominal dimensions but of different print layer orientations (i.e. $\theta = 0°$ and 90°), failed in different modes and fractured at different locations. A typical example is shown in Fig. 19, where it can be observed that the $\theta = 90°$ specimens failed by localised tearing while the $\theta = 0°$ specimen failed in shear-out, combined with significant curling. This is attributed to the fracture lines developing along the interface of adjoining print layers.

4.3. Ultimate loads and load-deformation responses

The ultimate loads P_u attained by all specimens are summarised in Table 7, while the load–displacement curves, all of which demonstrate good ductility, are plotted in Fig. 20. Note that the displacements (averaged from the two sides of the specimens) were measured over a gauge length of about 150 mm – see Fig. 8. Typical load–displacement curves of specimens exhibiting shear-out, net section tension, localised tearing, end-splitting and curl-bearing failures are presented in Fig. 21. It can be observed that, while the curves corresponding to specimens failing by shear-out, net section tension and end-splitting have one distinct peak, the curves of specimens failing by localised tearing and curl-bearing have two peaks. This phenomenon is associated with the occurrence of curling, which, as observed during the tests, corresponded to the initial drop in load (i.e. the first peak). Once significant curling had developed, the resistance increased until the attainment of the second peak triggered by localised fracture.

The influence of the geometric proportions of the lap plates on the load–displacement curves is presented in Fig. 22. As expected, increasing the plate width b was found to result in increasing ultimate capacities, as shown in Figs. 22(a) and 22(c) for the thinner (i.e. 3 mm)

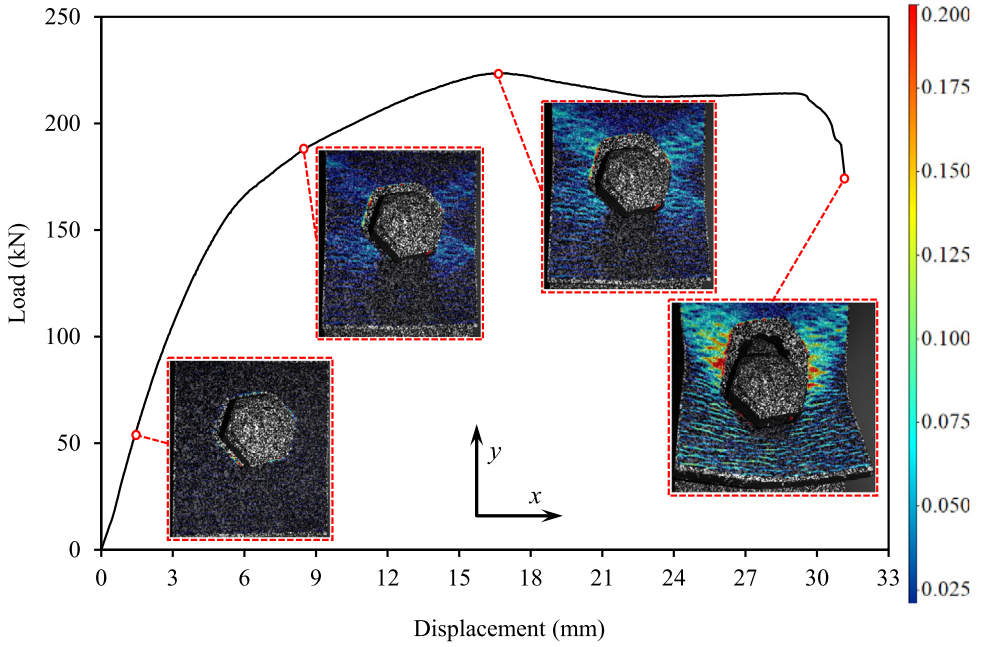

(a) Strain fields at different loading levels for the specimen

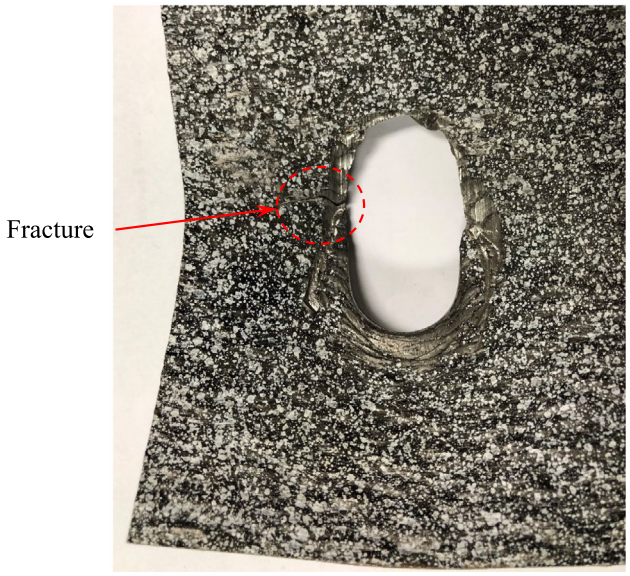

(b) Close-up view of the fracture

Fig. 11. Specimen (S8-117-80-90) failing by localised tearing.

and thicker (i.e. 8 mm) lap shear specimens respectively. Similarly, the influence of the end distance e_1 on the response of the lap shear specimens is illustrated in Figs. 22(b) and 22(d). It can be observed that the ultimate capacity of the specimens increased with increasing end distance, until the load–displacement curves began to exhibit two peaks, reflecting the development of significant curling, eventually leading to failure by localised tearing. It is therefore shown that when localised tearing governs, the influence of further increasing the end distance on the ultimate capacity of lap shear specimens is minimal.

The influence of the print layer orientation on the response of the lap shear specimens was not found to be significant. In Fig. 21, where the load–displacement curves plotted in each graph have the same geometry but different print layer orientations, all pairs of curves can be seen to follow similar trends with no significant differences. Comparisons of the ultimate capacities of the specimens with the same nominal geometry but of different print layer orientations (i.e. $P_{u,0}$ and $P_{u,90}$) are presented in Table 8. Since the actual plate thickness and ultimate tensile strength varied from their nominal values, the table also provides comparisons of the ultimate loads normalised by the product of the measured average thickness t and the ultimate tensile strength f_u, confirming the insensitivity of the connection performance to print layer orientation – see Table 8.

5. Existing design equations

The establishment of accurate and reliable design rules is important for the wider use of WAAM in construction. In this section, the resistances of the examined specimens, as determined by physical testing, are compared against the strength predictions given by the design equations set out in current steel design standards, namely AISI S100 [30], AISC 360 [31], Eurocode 3 [32,33] and AS/NZS 4600 [34], to assess their suitability for application to WAAM lap shear connections. Note

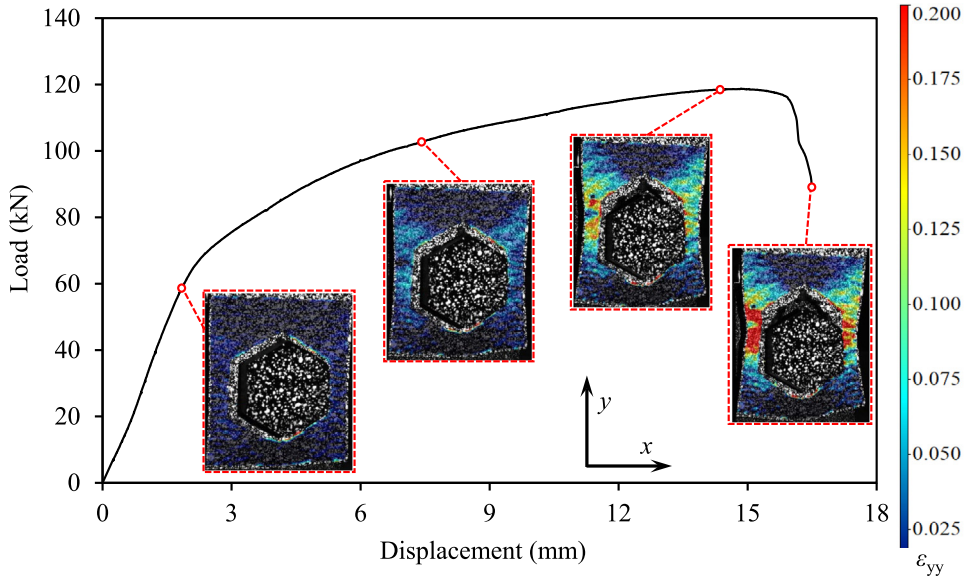

Fig. 12. Strain fields at different loading levels for a specimen (specimen S8-65-39-90) failing by net section tension.

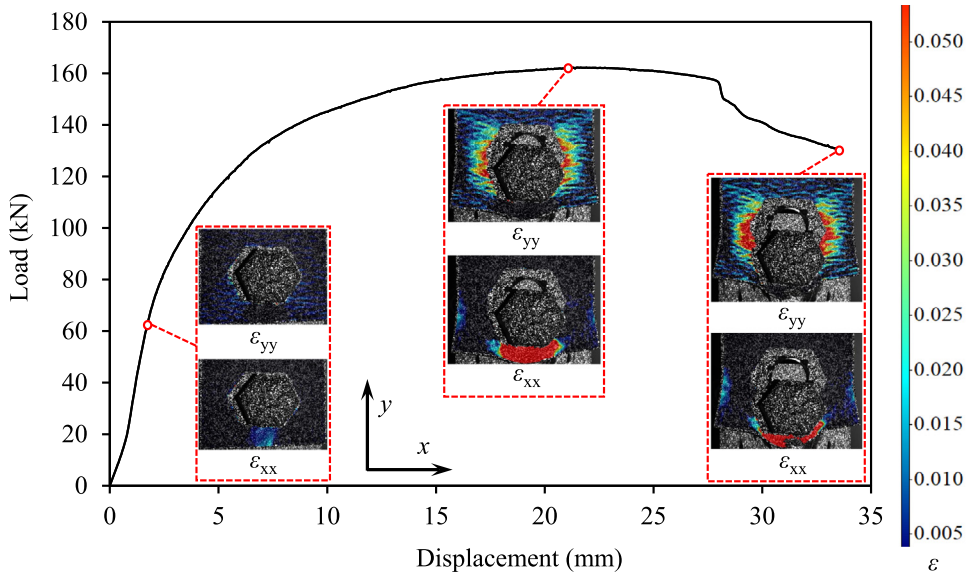

Fig. 13. Strain fields at different loading levels for a specimen (specimen S8-117-48-90) failing by end-splitting.

that the strength predictions used for the comparisons presented herein were derived using the measured geometric and material properties, while all safety factors were set equal to unity and are hence omitted from the presented formulae.

5.1. AISI S100

According to AISI S100-16 [30], when deformation around the bolt holes is not a design consideration, the bearing capacity $P_{b,AISI}$ of a bolted connection is given by Eq. (1):

$$P_{b,AISI} = C m_f d t f_u \tag{1}$$

where d is the diameter of the bolt, t is the average thickness of the test plate, f_u is the ultimate tensile strength, C is a bearing factor (equal to 3.0 for the specimens examined herein since $d/t < 10$) and m_f is a modification factor that depends on the type of connection (equal to 0.75 for lap shear connections without washers under single shear).

The nominal resistance of a lap shear connection failing by shear-out $P_{s,AISI}$ is given by Eq. (2),

$$P_{s,AISI} = 1.2 L_{nv} t f_u \tag{2}$$

while Eq. (3), introduced in [49], is adopted for the prediction of the resistance $P_{n,AISI}$ of a connection exhibiting net section tension failure.

$$P_{n,AISI} = A_n f_u (0.9 + \frac{0.1d}{b}) \tag{3}$$

The variable L_{nv} in Eq. (2) is the length of the net shear plane, as defined in Fig. 23. In Eq. (3), A_n is the net area of the connected plate and b is the width of the plate.

5.2. AISC 360

According to AISC 360-16 [31], when bolt hole deformation is not a concern, the bearing capacity $P_{b,AISC}$ is given by:

$$P_{b,AISC} = 3.0 d t f_u \tag{4}$$

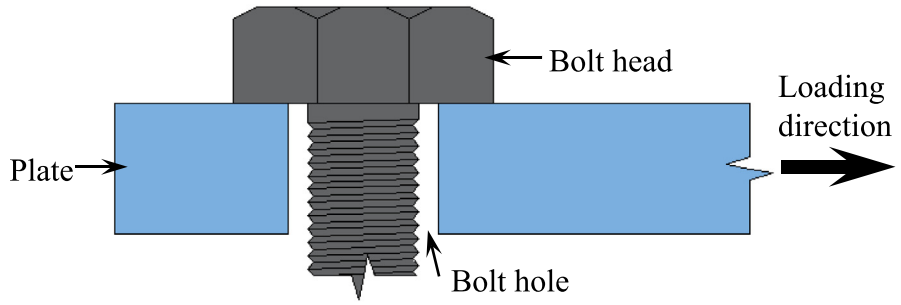

(a) Unloaded configuration

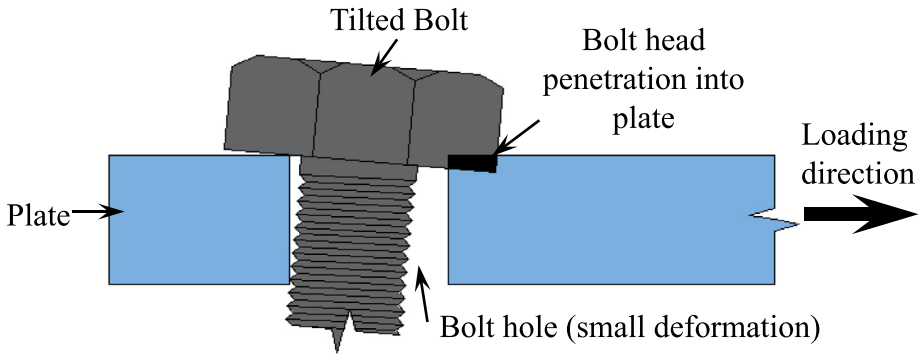

(b) Bolt head penetrating into plate during loading

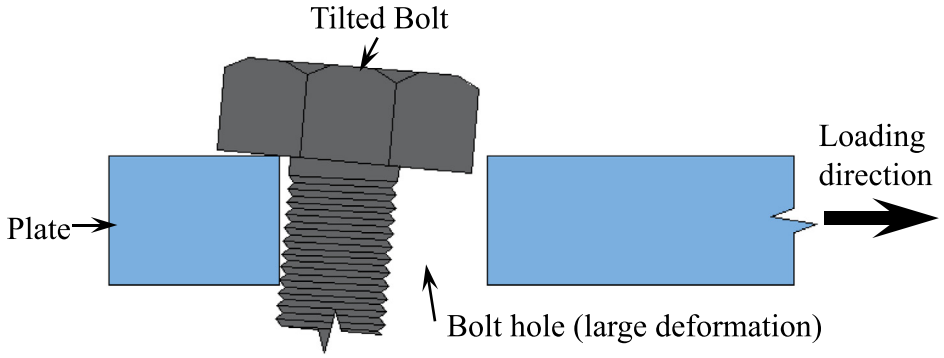

(c) Bolt head avoiding penetration into plate because of large deformation of bolt hole during loading

Fig. 14. Schematic view of bolt tilting and bolt head either penetration or avoiding plate in single-lap shear connections.

The shear-out capacity $P_{s,AISC}$ is given by:

$$P_{s,AISC} = 1.5 L_{nv} t f_u \tag{5}$$

and the net section tension capacity $P_{n,AISC}$ of a bolted connection is given by:

$$P_{n,AISC} = A_n f_u \tag{6}$$

5.3. Eurocode 3

According to the new draft EN 1993-1-8 [32], the ultimate capacity of a lap shear connection, as governed by bearing and shear-out failure, is given by Eq. (7):

$$P_{b,EC3} = k_m \alpha_b f_u d t \tag{7}$$

in which

$$\alpha_b = \min\left(\frac{e_1}{d_0}; 3\frac{f_{ub}}{f_u}; 3\right) \tag{8}$$

where k_m is a modification factor depending on the steel grade of the connected plate (which is equal to unity for steel grades lower than S460), e_1 is the end distance, as defined in Fig. 4, d_0 is the bolt hole diameter and f_{ub} is the ultimate tensile strength of the bolts.

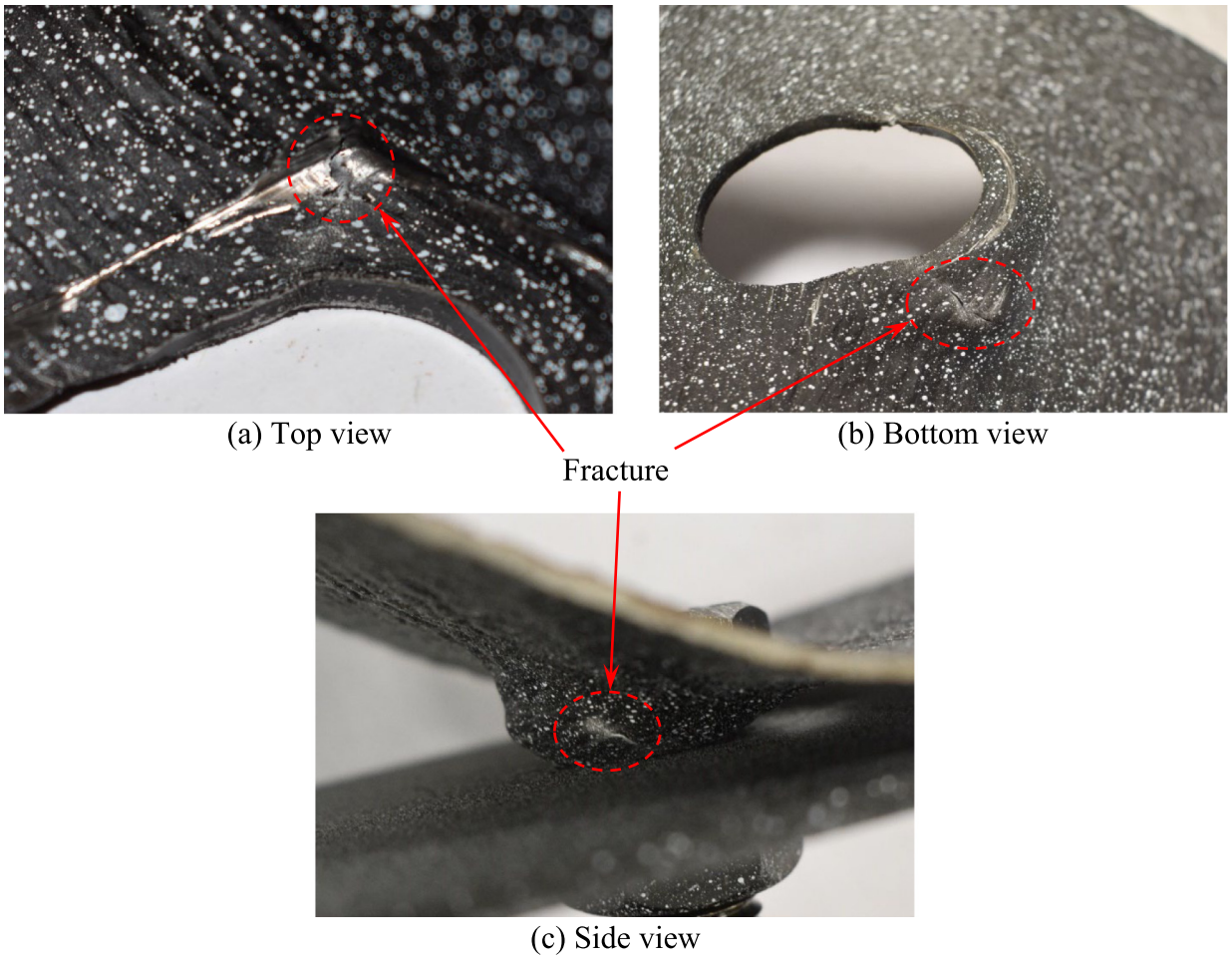

Fig. 15. Close-up view of bolt head penetrating into plate – curl-bearing failure (Specimen S3-145-104-90).

Fig. 16. Failure mode transition from net section tension to end-splitting and shear-out failure.

In the new draft EN 1993-1-1 [33], the net section tension resistance $P_{n,EC3}$ of a lap shear connection is defined as:

$$P_{n,EC3} = kA_n f_u \tag{9}$$

where k is equal to unity for plates with smooth bolt holes (i.e. fabricated by water jet cutting).

5.4. AS/NZS 4600

In AS/NZS 4600 [34], the resistances of lap shear connections to bearing and net section tension failure are predicted using the same equations as in AISI S100 [30] (i.e. Eqs. (1) and (3), respectively). The shear-out capacity $P_{s,AS/NZS}$ is predicted using Eq. (10) where, unlike

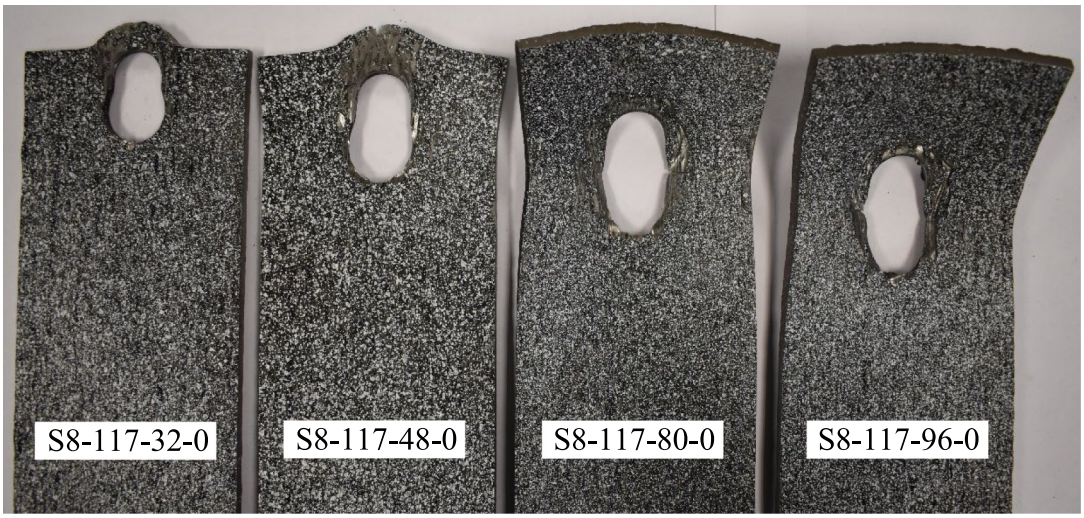

Fig. 17. Failure mode transition from shear-out to end-splitting and localised tearing failure.

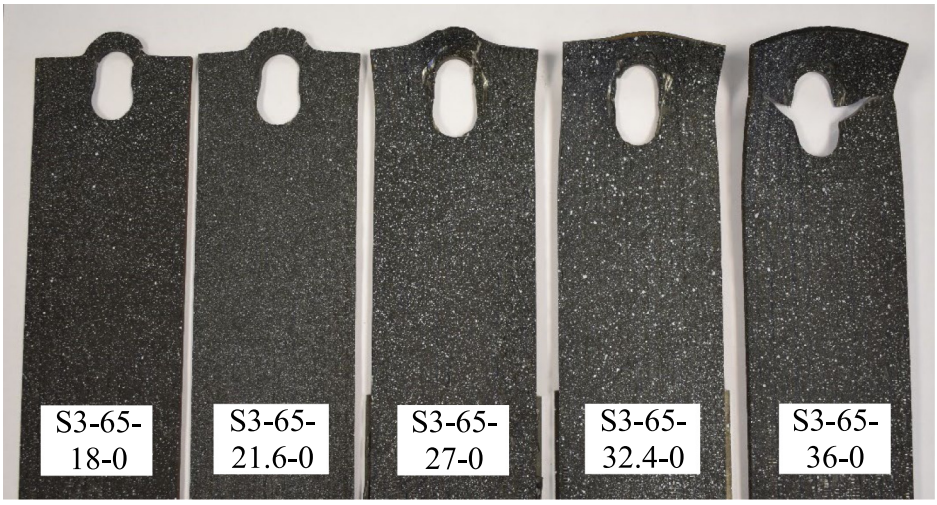

Fig. 18. Failure mode transition from shear-out to localised tearing failure.

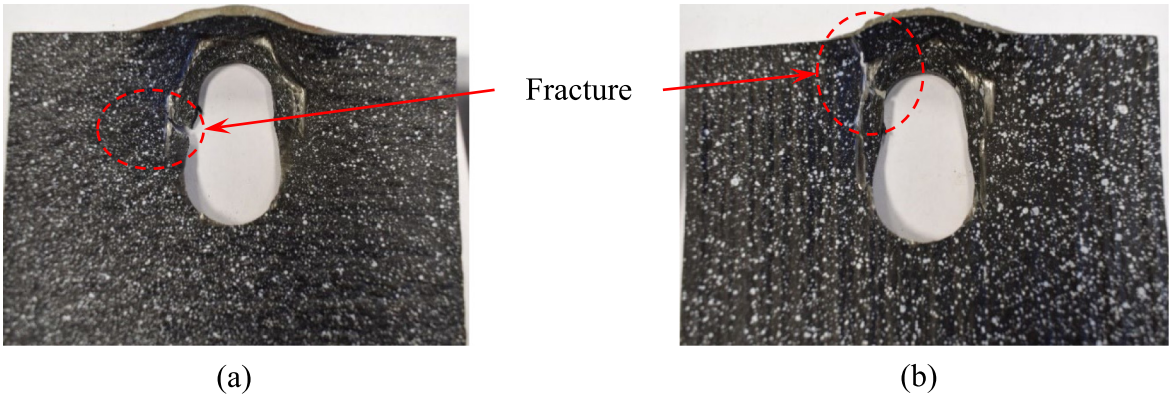

Fig. 19. (a) Localised tearing in specimen S3-105-33-90 and (b) shear-out failure in specimen S3-105-33-0.

the other specifications, the gross shear plane is employed:

$$P_{s,AS/NZS} = L_{gv} t f_u \tag{10}$$

where L_{gv} is the length of the gross shear plane, as defined in Fig. 23.

5.5. Design equations proposed in the literature

Further design expressions for predicting shear-out failure in lap shear connections have been proposed in the literature [45,50] and shown to yield accurate capacity predictions. Eq. (11) was proposed

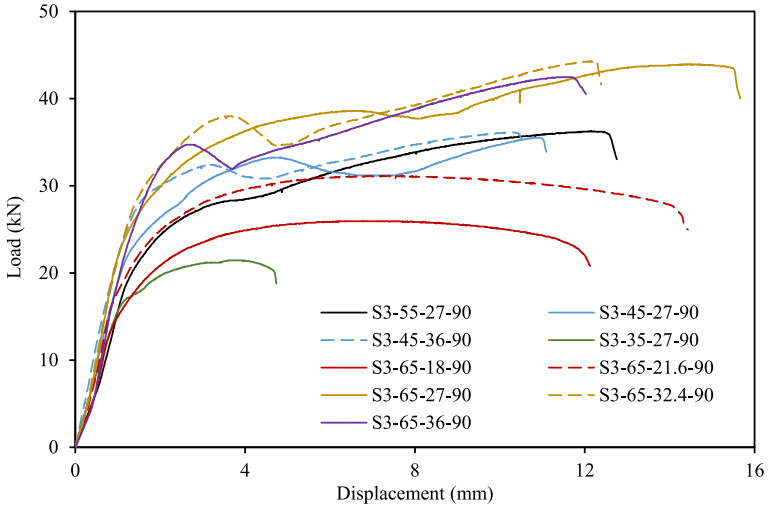

(a) t = 3mm, θ = 90° and b varying from 35 to 65 mm

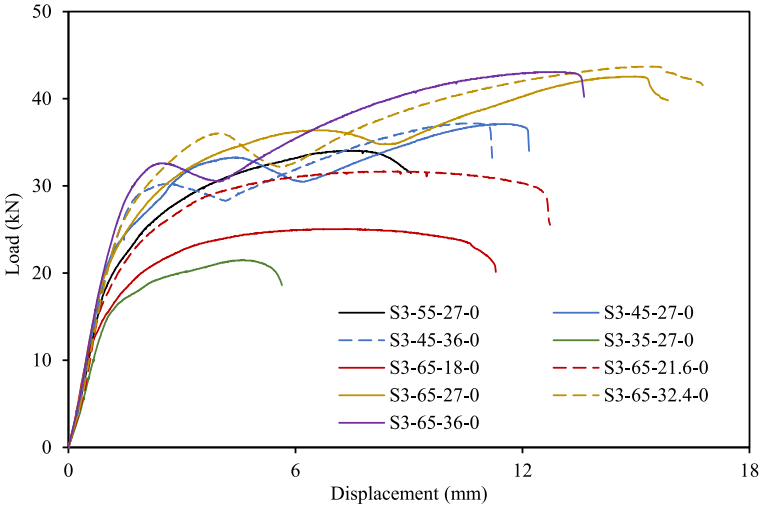

(b) t = 3mm, θ = 0° and b varying from 35 to 65 mm

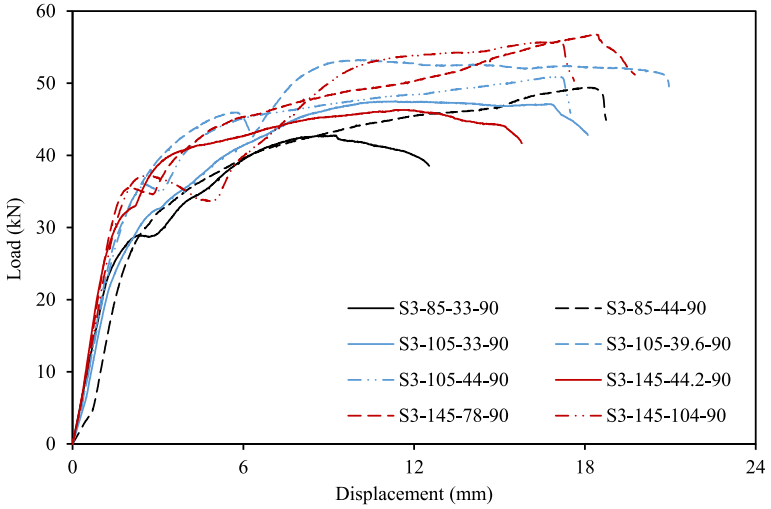

(c) t = 3mm, θ = 90° and b varying from 85 to 145 mm

Fig. 20. Load–displacement curves of lap shear test specimens.

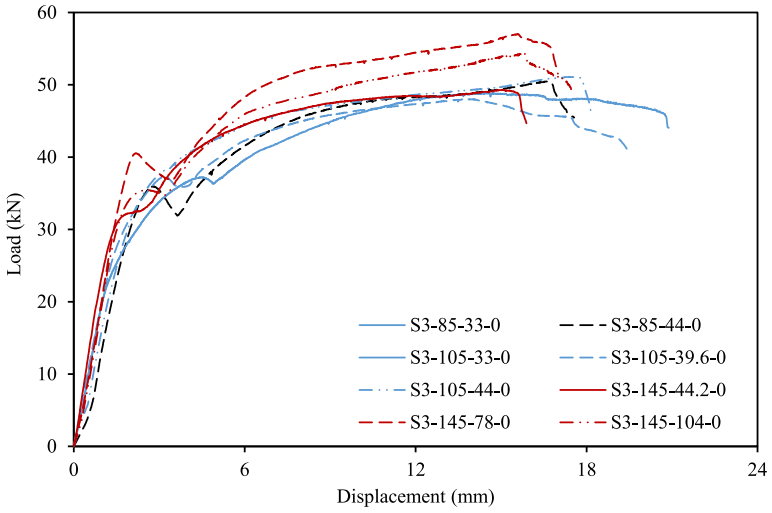

(d) t = 3mm, θ = 0° and b varying from 85 to 145 mm

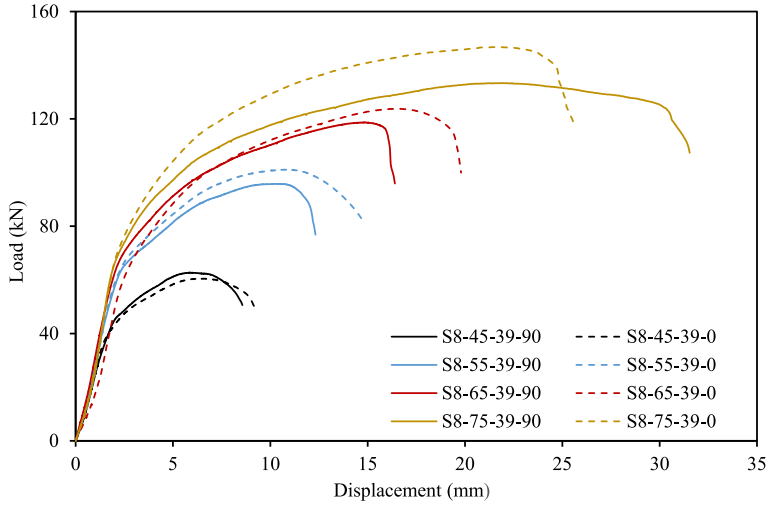

(e) t = 8 mm, θ = 90° and 0 and b varying from 45 to 75 mm

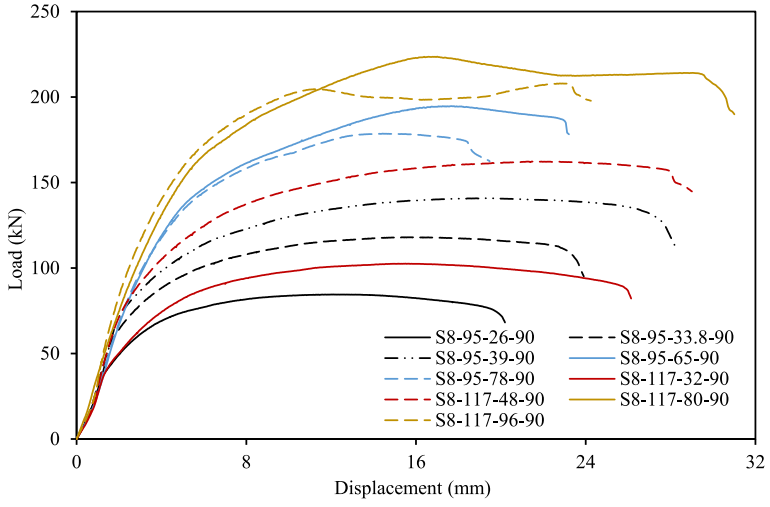

(f) t = 8 mm, θ = 90° and b varying from 95 and 117 mm

Fig. 20. (*continued*).

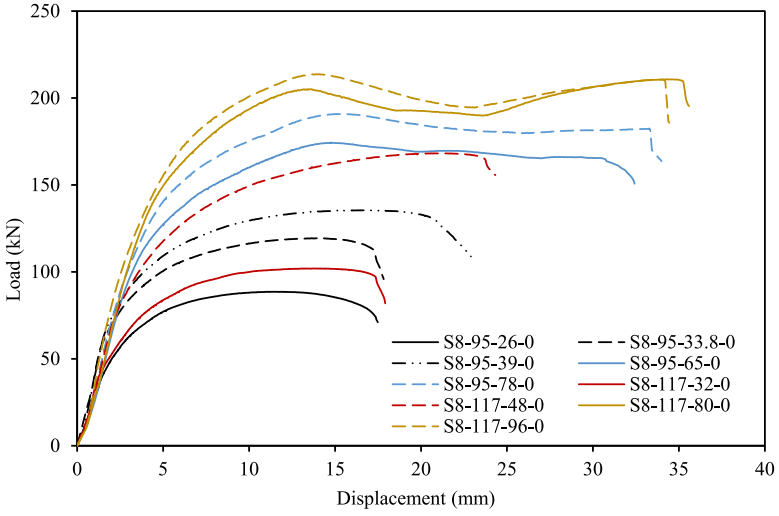

(g) $t = 8$ mm, $\theta = 0°$ and b varying from 95 and 117 mm

Fig. 20. (*continued*).

in [50] for the prediction of the ultimate shear-out resistance P_s:

$$P_s = 1.2 L_{av} t f_u \tag{11}$$

where L_{av} is the length of the active shear plane, assumed to lie between the gross and net shear planes, as illustrated in Fig. 23 and given by:

$$L_{av} = e_1 - \frac{d_0}{4} \tag{12}$$

For cold-reduced sheet steel bolted connections, Eq. (11) was modified [45] to give Eq. (13), which accounts for the catenary action that develops in specimens with short end distances:

$$P_s = 1.2\left(\frac{3d}{e_1}\right)^p L_{av} t f_u \tag{13}$$

in which the coefficient p is the catenary power, taken as 1/10 herein for the single-lap connections. A comparison between the predictions obtained using Eq. (13) for shear-out resistance and the test results is presented in Table 7.

Eq. (14) was proposed in [44] for determining the strength P_{tb} of single-lap shear bolted connections failing in tilt-bearing (i.e. the bolt head punching through the connected plate):

$$P_{tb} = 2.65 d^{1/2} t^{4/3} (b - d_0)^{1/6} f_u \tag{14}$$

Although tilt-bearing failure did not occur in the specimens examined herein, Eq. (14) can be used for predicting localised tearing and curl-bearing failure, as presented in Table 7.

6. Comparisons between test results and existing design equations

Comparisons between the test results and the capacity predictions given by the aforementioned design equations are presented in Table 7. The measured geometric and material properties shown in Tables 4 to 6 have been used in predicting the capacities. Note that the value of the tensile strength f_u used in the design equations was that determined from the material tests on the as-built coupons in the 0° and 90° directions depending on the print layer orientation of each specimen for both nominal material thicknesses (i.e. 3 mm and 8 mm), as reported in Table 6.

Among the current steel design standards, overall the most accurate capacity predictions were yielded by AS/NZS 4600 [34], with an average test-to-predicted capacity ratio of 1.02 in conjunction with a coefficient of variation (COV) of 0.11 – see Table 7. Although the equations of AISC 360 [31] led to an average capacity ratio of 0.99, the resulting COV is double that of the AS/NZS 4600 equations.

Table 8
Influence of print layer orientation on ultimate capacity of lap shear connections.

Specimen pair	$P_{u,90°}/P_{u,0°}$	$\frac{P_{u,90°}}{t f_{u,90°}} / \frac{P_{u,0°}}{t f_{u,0°}}$
S3-55-27	0.92	0.99
S3-45-27	0.96	1.03
S3-45-36	0.97	1.07
S3-35-27	1.00	1.05
S3-65-18	1.04	1.06
S3-65-21.6	0.98	1.05
S3-65-27	1.03	1.12
S3-65-32.4	1.01	1.04
S3-65-36	0.99	1.04
S3-85-33	0.88	0.94
S3-85-44	0.98	1.04
S3-105-33	1.00	1.02
S3-105-39.6	1.11	1.10
S3-105-44	1.00	1.02
S3-145-44.2	0.94	0.99
S3-145-78	1.00	1.07
S3-145-104	1.03	1.08
S8-45-39	1.04	1.04
S8-55-39	0.95	0.96
S8-65-39	0.96	1.00
S8-75-39	0.91	0.93
S8-95-26	0.95	0.95
S8-95-33.8	0.99	1.01
S8-95-39	1.04	1.03
S8-95-65	1.12	1.09
S8-95-78	0.93	0.93
S8-117-32	1.01	1.02
S8-117-48	0.96	0.98
S8-117-80	1.06	1.07
S8-117-96	0.97	1.00
Mean	0.99	1.02
COV	0.054	0.048

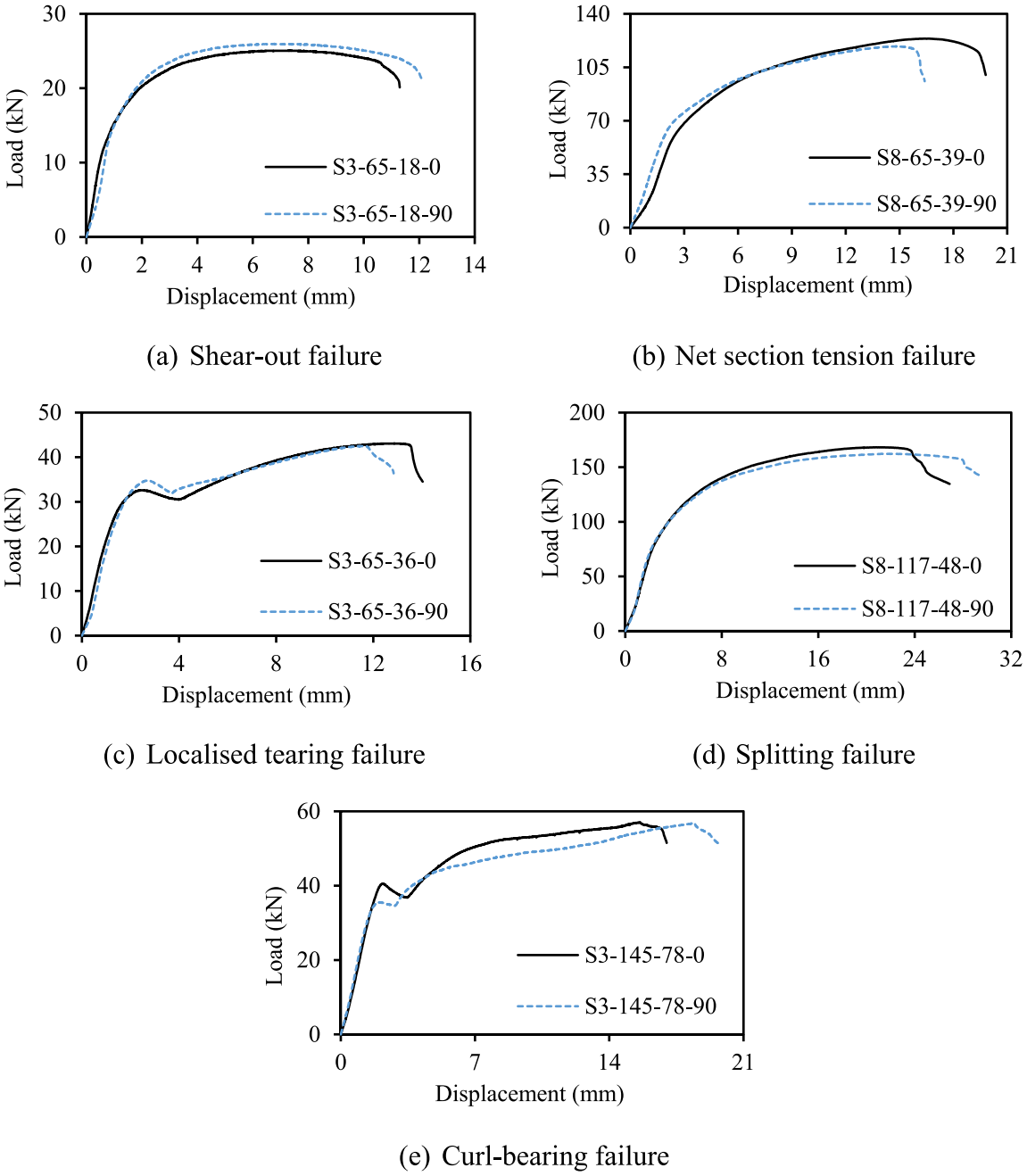

Fig. 21. Load–displacement curves of pairs of specimens with $\theta = 0°$ and $\theta = 90°$ exhibiting: (a) shear-out, (b) net section tension, (c) localised tearing, (d) end-splitting and (e) curl-bearing failure.

Overall, the AISI S100 equations [30] are the most conservative as they underestimated the capacity of the WAAM connections by 22% on average, with a COV of 0.21. Eurocode 3 [32,33] is the next most conservative, with an average test-to-predicted capacity ratio of 1.04 and a COV of 0.17.

Comparisons between design equations and test results that focus solely on the average test-to-predicted capacity ratios and the COV values can be misleading; further comparisons, based on failure modes, are therefore presented in the following sub-sections.

6.1. Net section tension failure

For the WAAM bolted connection test specimens undergoing net section tension (NS) failure, the four standards generally provide reasonable, if somewhat conservative (especially for the thicker specimens), capacity predictions. As shown in Fig. 24, the relevant equations of AISC [31] and Eurocode 3 [33], i.e. Eqs. (6) and (9), resulted in underestimations of net section tension capacity of up to 12% (1/1.13 = 0.88), while Eq. (3), specified in AISI [30] or AS/NZS [34], led to underestimations of up to 17% (1/1.20 = 0.83). The test-to-predicted capacity ratios of 1.27 and 1.28 shown in Table 7 for Specimens S8-65-39-90 and S8-65-39-0, respectively, were calculated using Eq. (2), since, according to AISI, shear-out (SO) was the critical failure mode. This result suggests that Eq. (2) is excessively conservative for connections failing in shear-out, as discussed in the following subsection.

6.2. Shear-out (and end-splitting) failure

Eqs. (2), (5) and (7), specified in AISI [30], AISC [31] and Eurocode 3 [32], respectively, generally provide overly conservative predictions

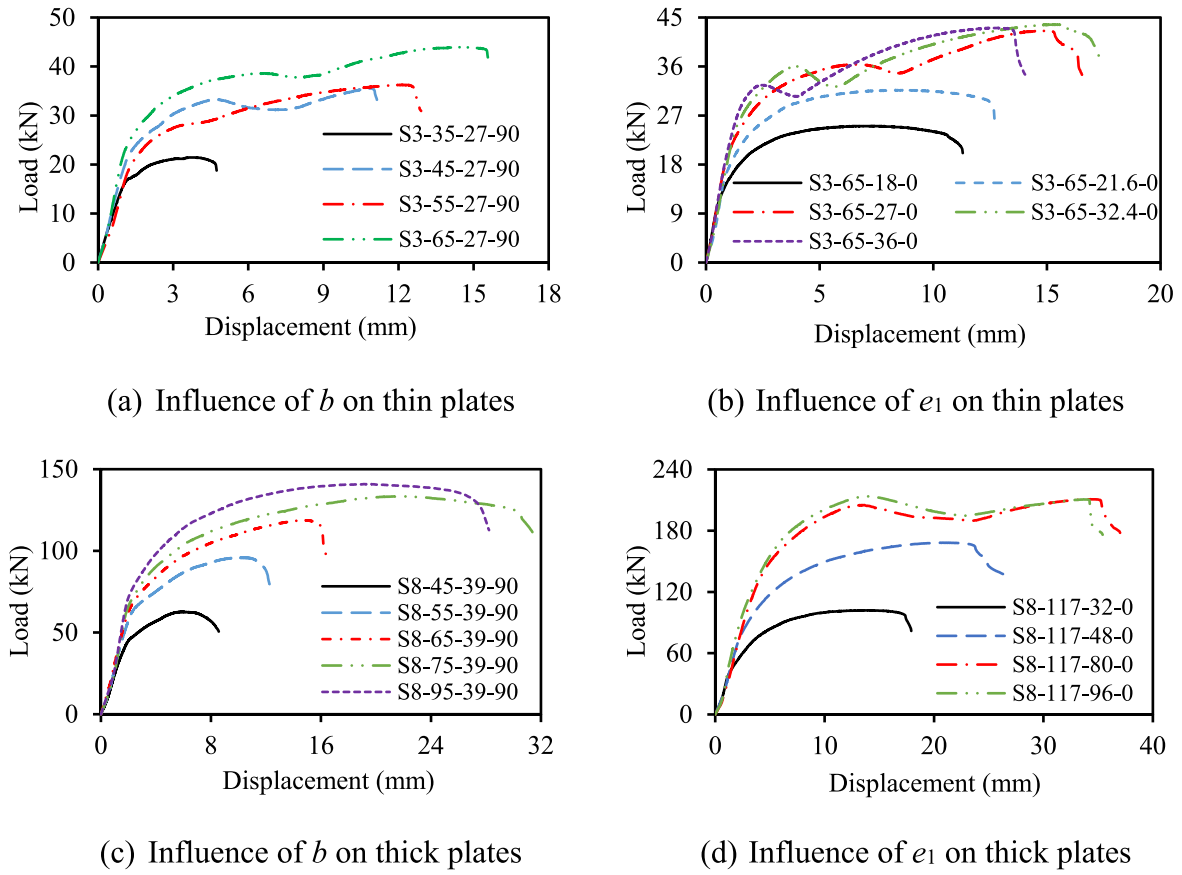

Fig. 22. Influence of width b and end distance e_1 on load–displacement curves of typical test specimens in comparison groups.

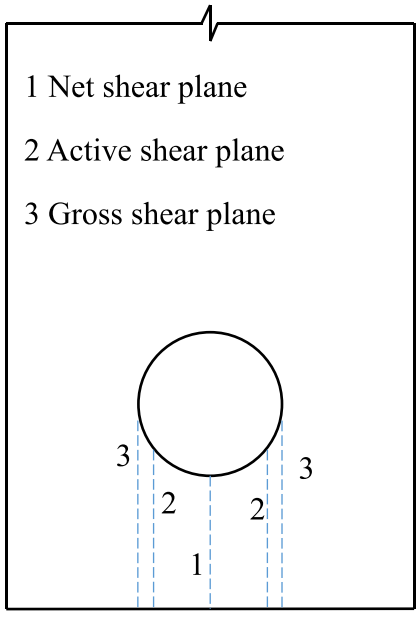

Fig. 23. Position of different shear planes.

of shear-out resistance, as evident from the results shown in Table 7 and Fig. 25. The greatest underestimations by AISI [30], AISC [31] and Eurocode [32] are 44% (1/1.79 = 0.56), 30% (1/1.43 = 0.70) and 25% (1/1.33 = 0.75), respectively. Eq. (10), specified in AS/NZS [34], is also conservative, but not to the same extent as the other specifications. The largest underestimation of 17% (1/1.20 = 0.83) is for Specimen S3-65-27-90, which failed in localised tearing.

It should be noted that, while an overestimation of capacity by a set of equations from a given design standard may simply indicate that the governing failure mode is not considered in that standard, any significant underestimation necessarily means that the available equation is too conservative. For example, Eurocode 3 [32] predicted that Specimen S3-65-27-90 would fail in shear-out (SO), but the specimen actually failed in localised tearing at an ultimate load that was 33% higher than the predicted shear-out capacity. This result means that the actual shear-out capacity must be more than 33% greater than the predicted capacity since the specimen was stronger in shear-out than in localised tearing.

The accuracy of the shear-out capacity predictions of the standards could be improved through the incorporation of Eq. (13). It can be seen that this equation generally predicted the test shear-out (SO) capacities to within 5%. Using Eq. (13) for the shear-out capacity prediction of Specimen S3-105-33-0 results in a test-to-predicted capacity ratio of 1.04, instead of 1.39 [30], 1.11 [31,34] or 1.22 [32] from the considered standards. Similar observations can be made for other specimens failing in shear-out such as Specimens S3-65-18-90 and S8-95-39-90. For practical purposes, it is also proposed that Eq. (13) may be used for estimating both shear-out and the end-splitting (ES) capacities, owing to their similarity – see Table 7.

6.3. Localised tearing and curl-bearing failures

As shown in Table 7 and Figs. 24 and 25, AISC [31], AS/NZS [34] and Eurocode [32,33] can either underestimate or overestimate the localised tearing (LT) capacities of the test specimens significantly. The underestimations are generally due to the conservatism of the shear-out

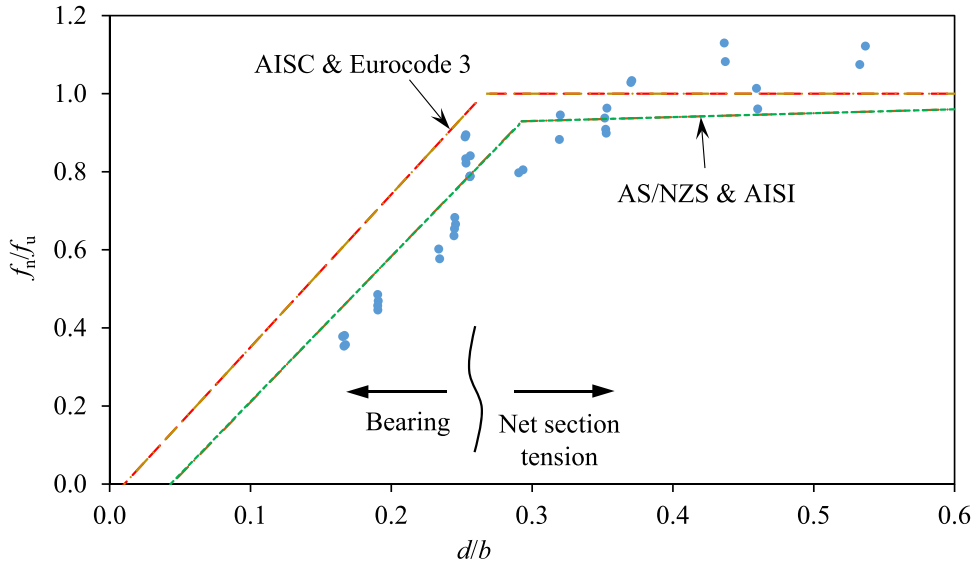

Fig. 24. Comparison of experimental results and design equations for bearing and net section tension, where net section tension and bearing failure, as described by the considered design codes, are indicated.

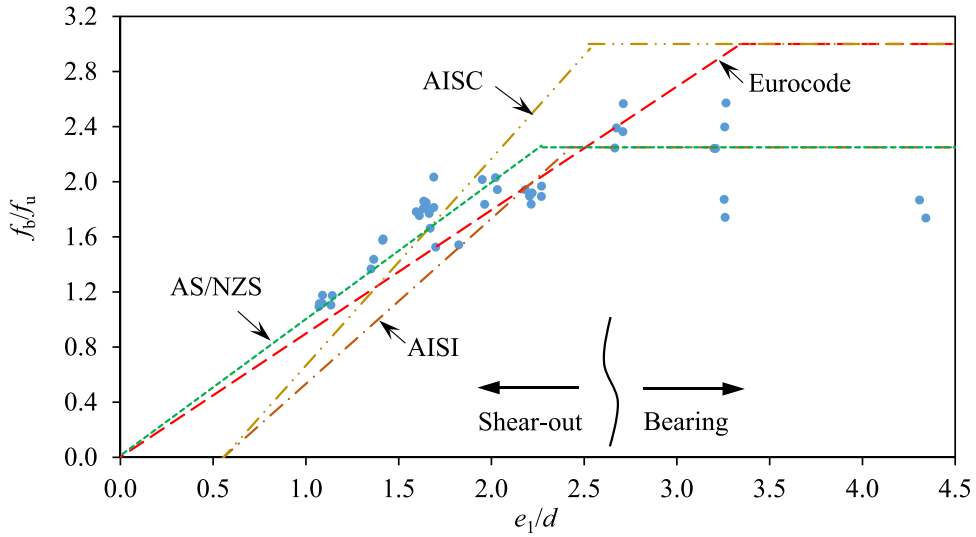

Fig. 25. Comparison of experimental results and design equations for shear-out and bearing, where shear-out and bearing failure, as described by the considered design codes, are indicated.

design provisions (especially for AISI [30]), while the overestimations are due to the fact that the localised tearing mode is not properly considered by the standards.

The curl-bearing failure mode is not accounted for in current design standards; hence, all the standards overestimate the curl-bearing (CB) capacities significantly, by at least 20% (1/0.83 = 1.20) and up to 72% (1/0.58 = 1.72). These results demonstrate the need to assess the suitability of a design equation or a set of design equations not only based on the average test-to-predicted capacity ratios, but also considering the performance of particular specimens and failure modes.

The last column of Table 7 contains the results of using Eq. (14) to predict the capacities of the specimens failing in localised tearing or curl-bearing. Although the equation was originally derived for the tilt-bearing failure mode [44], it has transpired that it can be used to conservatively estimate the localised tearing or curl-bearing failure load of the tested WAAM specimens, mostly within 10% accuracy. The unexpected level of accuracy is due to the fact that both the localised tearing and curl-bearing failure modes involve through-thickness fracture of the connected plate under the bolt head, as in the case of the tilt-bearing failure mode.

If Equation (14) were to be incorporated into the sets of equations specified in the considered design standards, then each of the design standards would yield a test-to-predicted capacity ratio of 1.05 for the curl-bearing Specimen S3-145-104-0, instead of 0.77 [30,34] or 0.58 [31,32]. For the localised tearing Specimen S3-65-36-0, the incorporation of Eq. (14) would lead to a test-to-predicted capacity ratio of 1.06 instead of 0.92 [30], 0.74 [31], 0.84 [34] or 0.93 [32].

7. Conclusions

A total of 60 WAAM steel single-lap shear bolted connections of two different nominal thicknesses, two different print layer orientations and varying dimensions were tested. The measured material properties, geometries, load-deformation characteristics and failure modes, including shear-out, localised tearing, curl-bearing and net section tension fracture, of the test specimens are reported and analysed. The test ultimate loads were compared against the predictions of four major design standards for either structural/hot-rolled (AISC 360 and EN 1993-1-8) or cold-formed (AISI S100 and AS/NZS 4600) steel.

The experimental programme revealed that the print layer orientation had little influence on the deformation and load-carrying capacities of the WAAM connections. Although the failure mode sometimes depended on the print layer orientation, the ultimate test loads were essentially unaffected. This finding means that the same structural design equations can be used for different print layer orientations.

The ductility of the WAAM steel enabled the bolt hole of each specimen to elongate to a sufficient extent so that the bolt head avoided punching through the connected plate upstream, i.e. no tilt-bearing failures occurred. Specimens with sufficiently large end distances (to avoid shear-out) and widths (to avoid net section tension fracture) failed predominantly in localised tearing. However, specimens with larger end distances experienced curling which was so severe that the bolt head punched through the connected plate downstream of the bolt hole, as the bolt displaced in the loading direction. To the author's knowledge, this is the first time that this failure mode is identified and is defined as curl-bearing failure.

Current steel design standards were found to not adequately account for the localised tearing and the curl-bearing failure modes; the failure loads of specimens failing in these modes were therefore generally poorly predicted. However, the localised tearing and curl-bearing failure modes have a similar fracture mechanism to the tilt-bearing failure mode, and the corresponding failure loads are reasonably well predicted by a previously proposed equation [44] for tilt-bearing failure.

Overall, the WAAM test specimens exhibited the anticipated behavioural trends and, notwithstanding the above shortcomings, their failure loads were generally well predicted by the existing design standards, with AS/NZS 4600 providing the most accurate capacity predictions. Further research is required to assess reliability and to derive suitable safety factors for use in the design of WAAM connections.

CRediT authorship contribution statement

Xi Guo: Writing – review & editing, Writing – original draft, Visualization, Validation, Software, Methodology, Investigation, Formal analysis, Data curation. **Pinelopi Kyvelou:** Writing – review & editing, Visualization, Validation, Supervision, Software, Methodology, Investigation, Data curation, Conceptualization. **Jun Ye:** Writing – review & editing, Software, Methodology, Investigation, Conceptualization. **Lip H. Teh:** Writing – review & editing, Validation, Supervision, Methodology, Investigation. **Leroy Gardner:** Writing – review & editing, Validation, Supervision, Resources, Project administration, Methodology, Investigation, Funding acquisition, Conceptualization.

Declaration of competing interest

The authors declare the following financial interests/personal relationships which may be considered as potential competing interests: Leroy Gardner reports financial support was provided by Horizon 2020.

Data availability

Data will be made available on request.

Acknowledgements

This research was possible thanks to funding and support from the European Union's Horizon 2020 research and innovation programme under grant agreement No. 820776 'Intelligent data-driven pipeline for the manufacturing of certified metal parts through Direct Energy Deposition process INTEGRADDE'. The authors also would like to acknowledge the contribution of MX3D for the fabrication of the test specimens and Gordon Herbert and Harry Slack at Imperial College London for their assistance in the programme.

References

[1] L. Gardner, P. Kyvelou, G. Herbert, C. Buchanan, Testing and initial verification of the world's first metal 3D printed bridge, J. Construct. Steel Res. 172 (2020) 106233.
[2] N. Hadjipantelis, B. Weber, C. Buchanan, L. Gardner, Description of anisotropic material response of wire and arc additively manufactured thin-walled stainless steel elements, Thin-Walled Struct. 171 (2022) 108634.
[3] V. Laghi, M. Palermo, L. Tonelli, G. Gasparini, L. Ceschini, T. Trombetti, Tensile properties and microstructural features of 304L austenitic stainless steel produced by wire and arc additive manufacturing, Int. J. Adv. Manuf. Technol. 106 (2020) 3693–3705.
[4] V.A. Silvestru, I. Ariza, J. Vienne, L. Michel, A.M. Aguilar Sanchez, U. Angst, R. Rust, F. Gramazio, M. Kohler, A. Taras, Performance under tensile loading of point-by-point wire and arc additively manufactured steel bars for structural components, Mater. Des. 205 (2021) 109740.
[5] F. Martina, J. Mehnen, S.W. Williams, P. Colegrove, F. Wang, Investigation of the benefits of plasma deposition for the additive layer manufacture of Ti–6Al–4V, J. Mater. Process. Tech. 212 (6) (2012) 1377–1386.
[6] P. Kyvelou, C. Huang, L. Gardner, C. Buchanan, Structural testing and design of wire arc additively manufactured square hollow sections, J. Struct. Eng. 147 (2021) 1–19.
[7] C. Buchanan, L. Gardner, Metal 3D printing in construction: A review of methods, research, applications, opportunities and challenges, Eng. Struct. 180 (2019) 332–348.
[8] P. Kyvelou, H. Slack, D.D. Mountanou, M.A. Wadee, T.B. Britton, C. Buchanan, L. Gardner, Mechanical and microstructural testing of wire and arc additively manufactured sheet material, Mater. Des. 192 (2020) 108675.
[9] A. Kanyilmaz, A.G. Demir, M. Chierici, F. Berto, L. Gardner, S.Y. Kandukuri, P. Kassabian, T. Kinoshita, A. Laurenti, I. Paoletti, A. du Plessis, S.M.J. Razavi, Role of metal 3D printing to increase quality and resource-efficiency in the construction sector, Addit. Manuf. 50 (2022) 102541.
[10] J. Ye, P. Kyvelou, F. Gilardi, H. Lu, M. Gilbert, L. Gardner, An end-to-end framework for the additive manufacture of optimized tubular structures, IEEE Access 9 (2021) 165476-165489.
[11] G. Winter, Tests on bolted connections in light gage steel, J. Struct. Div. 82 (2) (1956) 1–25.
[12] M. D'Antimo, J.F. Demonceau, J.P. Jaspart, M. Latour, G. Rizzano, Experimental and theoretical analysis of shear bolted connections for tubular structures, J. Constr. Steel Res. 138 (2017) 264–282.
[13] M. Latour, G. Rizzano, Numerical study on the resistance of thread-fixed one-side bolts: Tensile and bearing strength, Structures 32 (2021) 958–972.
[14] M. Latour, G. Rizzano, M. D'Antimo, J.F. Demonceau, J.P. Jaspart, V. Armenante, Bearing strength of shear connections for tubular structures: An analytical approach, Thin-Walled Struct. 127 (2018) 180–199.
[15] R.A. Laboube, Strength of bolted connections: is it bearing or net section?, in: 9th Int. Specialty Conf. on Cold-Formed Steel Struct., 1988, pp. 589–601.
[16] F. Zadanfarrokh, E.R. Bryan, Testing and design of bolted connections in cold formed steel sections, in: 11th Int. Specialty Conf. on Cold-Formed Steel Struct., 1992, pp. 625–662.
[17] C.A. Rogers, G.J. Hancock, Bolted connection tests of thin G550 and G300 sheet steels, J. Struct. Eng. 125 (2) (1998) 128–136.
[18] C.A. Rogers, G.J. Hancock, Bolted connection design for sheet steels less than 1.0 mm thick, J. Constr. Steel Res. 51 (2) (1999) 123–146.
[19] C.A. Rogers, G.J. Hancock, Failure modes of bolted-sheet-steel connections loaded in shear, J. Struct. Eng. 126 (3) (2000) 288–296.
[20] J.A. Wallace, R.M. Schuster, Testing of bolted cold-formed steel connections in bearing (with and without washers), in: 16th Int. Specialty Conf. on Cold-Formed Steel Struct., 2002, pp. 730–747.
[21] R. Puthli, O. Fleischer, Investigations on bolted connections for high strength steel members, J. Constr. Steel Res. 57 (3) (2001) 313–326.
[22] P. Može, D. Beg, High strength steel tension splices with one or two bolts, J. Constr. Steel Res. 66 (8–9) (2010) 1000–1010.
[23] Y. Wang, Y. Lyu, G. Li, Experimental investigation of two-bolt connections for high strength steel members, in: 12th Int. Conf. on Advances in Steel-Concrete Composite, 2018, pp. 595–600.
[24] T.S. Kim, H. Kuwamura, Finite element modeling of bolted connections in thin-walled stainless steel plates under static shear, Thin-Walled Struct. 45 (4) (2007) 407–421.
[25] E.L. Salih, L. Gardner, D.A. Nethercot, Numerical investigation of net section failure in stainless steel bolted connections, J. Constr. Steel Res. 66 (12) (2010) 1455–1466.
[26] E.L. Salih, L. Gardner, D.A. Nethercot, Bearing failure in stainless steel bolted connections, Eng. Struct. 33 (2011) 549–562.
[27] J.S. Lim, T.S. Kim, S.H. Kim, Ultimate strength of single shear bolted connections with cold-formed ferritic stainless steel, J. Zhejiang Univ. Sci. A (Appl. Phys. Eng.) 14 (2) (2013) 120–136.
[28] Z. Wong, Y. Wang, X. Yun, L. Gardner, L.H. Teh, Experimental study of swage-locking pinned aluminium alloy shear connections, Thin-Walled Struct. 163 (2021) 107641.

[29] T.S. Kim, H. Kuwamura, T.J. Cho, A parametric study on ultimate strength of single shear bolted connections with curling, Thin-Walled Struct. 46 (2008) 38–53.
[30] AISI, North American specification for the design of cold-formed steel structural members, AISI S100-16w/S1-18, American Iron and Steel Institue, Washington DC, 2016.
[31] AISC, Specification for structural steel buildings, ANSI/AISC 360-16, American Institute of Steel Construction, Chicago, 2016.
[32] Eurocode 3: Design of Steel Structures – Part 1-8: Design of Joints, PrEN 1993-1-8, European Committee for Standardisation, Brussels, 2021.
[33] Eurocode 3: Design of Steel Structures – Part 1-1: General Rules and Rules for Builidng, PrEN 1993-1-1, European Committee for Standardisation, Brussels, 2020.
[34] AS/NZS, Cold-Formed Steel Structures, AS/NZS 4600:2018, Australian/New Zealand Standard, Sydney, 2018.
[35] MX3D, About – MX3D, 2021, [online] Available from https://mx3d.com, accessed Mar. 15, 2021.
[36] EN ISO 14341: 2020 Welding consumables – Wire electrodes and weld deposits for gas shielded metal arc welding of non alloy and fine grain steels-Classification, International Organization for Standardization.
[37] FARO design ScanArm 2.0®, 2018.
[38] 3D Systems, Geomagic Wrap 2017 (Version 2017.0.2:64) [Software] 2017 3D Systems, Incorporated and its licensors, 2017.
[39] Rhino 3D, Rhino 3D Computer-Aided Design Software (Version 5 SR14 64-Bit) [Software] Robert McNeel & Associates, 2017.
[40] EN ISO 6892-1: 2019 Meallic materials – tensile testing, part1: Method of test at room temperature, International Organization for Standardization.
[41] LaVision, DaVis (Version 8.4.0) [Software] la Vision GmbH, 2017.
[42] C. Huang, P. Kyvelou, R. Zhang, T.B. Britton, L. Gardner, Mechanical testing and microstructure of wire arc additively manufactured steels, Mater. Des. 216 (2021) 110544.
[43] A. Talja, M. Torkar, Lap shear tests of bolted and screwed ferritic stainless steel connections, Thin-Walled Struct. 83 (2014) 157–168.
[44] L.H. Teh, M.E. Uz, Ultimate tilt-bearing capacity of bolted connections in cold-reduced steel sheets, J. Struct. Eng. 143 (4) (2017) 04016206.
[45] H. Xing, L.H. Teh, Z. Jiang, A. Ahmed, Shear-out capacity of bolted connections in cold-reduced steel sheets, J. Struct. Eng. 146 (4) (2020) 04020018.
[46] Y. Wang, Y. Lyu, G. Li, J.Y.R. Liew, Behavior of single bolt bearing on high strength steel plate, J. Constr. Steel Res. 137 (2017) 19–30.
[47] C.O. Rex, W.S. Easterling, Behavior and modeling of a bolt bearing on a single plate, J. Struct. Eng. 129 (6) (2003) 792–800.
[48] P. Može, D. Beg, A complete study of bearing stress in single bolt connections, J. Constr. Steel Res. 95 (2014) 126–140.
[49] L.H. Teh, B.P. Gilbert, Net section tension capacity of bolted connections in cold-reduced steel sheets, J. Struct. Eng. 138 (3) (2012) 337–344.
[50] L.H. Teh, M.E. Uz, Ultimate shear-out capacities of structural-steel bolted connections, J. Struct. Eng. 141 (6) (2015) 04014152.